

4 M 80  
M-37-65-1  
C-5-P

M-37-65-1 - MARCH 1965

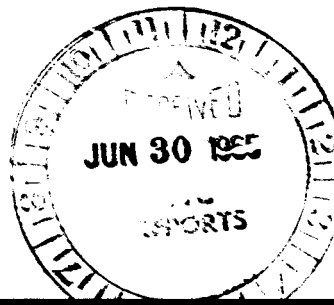
M-37-65-1

SHEET LISTED

THE AEROELASTIC CHARACTERISTICS  
OF THE SATURN-IB AND SATURN-V  
LAUNCH VEHICLES

GPO PRICE \$ \_\_\_\_\_  
CFSTI PRICE(S) \$ \_\_\_\_\_  
Hard copy (HC) \$ 3.00  
Microfiche (MF) .75

ff 653 July 65



FACILITY FORM 602

ACCESSION NUMBER	N66-26820	(THRU)
PAGES	79	
CR-75301		(CODE)
		31
		(CATEGORY)

THE AEROELASTIC  
CHARACTERISTICS OF THE SATURN-IB  
AND SATURN-V LAUNCH VEHICLES

March 1965

*J. Peter Reding*  
J. Peter Reding  
Aero-Hydrodynamics

*N J French*  
Norman J. French  
Aero-Hydrodynamics

*D M Jecmen*  
Dennis M. Jecmen  
Aero-Hydrodynamics

*Lars-Eric Ericsson*  
Lars-Eric Ericsson  
Flight Technology

APPROVED: *M. Tucker*  
M. Tucker, Manager  
Flight Technology

Prepared Under Contract NAS 8-11238  
for  
Aerodynamic Division  
Aero-Astrodynamic Laboratory  
George C. Marshall Space Flight Center  
National Aeronautics and Space Administration  
Huntsville, Alabama

## ABSTRACT

*2/1/69*

The effects of flow separation on the aeroelastic characteristics of the Saturn-IB and Saturn-V launch vehicles with an Apollo payload have been investigated. The steady and unsteady aerodynamic loads over these vehicles are dominated by separated flow. The results of a single-degree-of-freedom, quasi-steady analysis of the first three, free-free, body bending modes indicate that both vehicles are aerodynamically damped over the high-dynamic-pressure portions of their trajectories ( $0.8 \leq M \leq 2.0$ ). Thus, one can conclude that both vehicles will be aerodynamically damped over the entire ascent Mach-number range.

## SUMMARY

Certain geometric features common to many manned boosters, such as tower-mounted escape rockets and steep interstage flares, are sources of flow separation that may dominate the vehicle dynamics in the transonic Mach-number range where the dynamic pressure is large. Such is the case with the Saturn-Apollo manned boosters. A quasi-steady analysis technique, which uses the static experimental load distribution as an input, has been used to obtain the aerodynamic damping for the first three bending modes of the Saturn-IB and Saturn-V vehicles.

The analytical results indicate that the Saturn-IB and Saturn-V vehicles are aerodynamically damped over the critical Mach-number range ( $0.8 \leq M \leq 2.0$ ). Therefore, one may expect both vehicles to be damped over the entire ascent Mach-number range. An analysis of an additional Saturn I - Apollo configuration (flights SA-8 and SA-9) is documented in Appendix B. Positive aerodynamic damping is predicted also for this vehicle.

## CONTENTS

Section	Page
ABSTRACT	iii
SUMMARY	v
ILLUSTRATIONS	ix
1 INTRODUCTION	1-1
2 MECHANICS OF SEPARATED FLOW	2-1
2.1 Separated-Flow Aerodynamics	2-1
2.2 Quasi-Steady Loads	2-8
3 SATURN-APOLLO ANALYSIS	3-1
3.1 Static Aerodynamic Analysis	3-3
3.2 Aerodynamic Damping Analysis	3-4
4 CONCLUSIONS	4-1
5 RECOMMENDATIONS FOR FURTHER STUDY	5-1
6 REFERENCES	6-1
Appendix	
A NOTATION	A-1
B ANALYSIS OF THE SATURN-I (SA-8 AND SA-9) CONFIGURATION	B-1
C DOCUMENTATION OF SATURN-IB LUMPED LOADS	C-1
D DOCUMENTATION OF SATURN-V LUMPED LOADS	D-1

## ILLUSTRATIONS

Figure		Page
1-1	Saturn-V Flow Field at $M = 1.46$	1-2
2-1	Command-Module, Attached and Separated-Flow Loads at $M = 1.0$	2-2
2-2	Comparison of Nondirecting and Directing Wake-Source Configurations	2-5
2-3	Shock-Induced Loads	2-6
2-4	Effect of Boundary-Layer Thickening on Shock Position	2-7
2-5	Quasi-Steady Wake-Source Flow Models	2-9
2-6	Quasi-Steady Shock-Induced Separation Flow Model	2-11
3-1	Aerodynamic Damping at $\alpha = 0^\circ$ of the Saturn I-Apollo Vehicle With Escape Rocket (Disk Off)	3-2
3-2	Saturn-IB and Saturn-V Service Module Loads at $\alpha = 0^\circ$	3-7
3-3	Saturn-IB and Saturn-V Service Module - S-IVB Interstage Frustum Loads at $\alpha = 0^\circ$	3-8
3-4	Saturn-IB and Saturn-V Command-Module Loads at $\alpha = 0^\circ$	3-9
3-5	Saturn-Apollo Configurations	3-10
3-6	Comparison of Saturn-IB Integrated Lumped Loads With Force Data Results at $\alpha = 0^\circ$	3-11
3-7	Comparison of Saturn-V Lumped Loads and Force Data Results at $\alpha = 0^\circ$	3-12
3-8	Correlation of Saturn-IB Static and Dynamic Separated-Flow Loads at $M = 1.2$	3-13
3-9	Comparison of Saturn-Apollo Damping Characteristics at $\alpha = 0^\circ$	3-14
3-10	Comparison of Static and Dynamic Characteristics of the Service Module - S-IVB Interstage Loads	3-15
3-11	Effects on the Saturn-Apollo 1st Mode Damping of the Service Module - S-IVB Interstage Loads	3-16
3-12	Effects on the Saturn-Apollo 3rd Mode Damping of the Command Module and Forward Service Module Loads	3-17

Figure		Page
3-13	Saturn-IB Aerodynamic Damping	3-18
3-14	Saturn-V Aerodynamic Damping	3-19
B-1	Saturn-I (SA-8 and SA-9) Configuration	B-2
B-2	Saturn-I Service Module – S-IV Interstage Frustum Loads	B-3
B-3	Saturn I-Apollo (SA-8 and SA-9) Damping at $\alpha = 0^\circ$	B-4
C-1	Saturn-IB, Definition of Lumped Normal Force Vectors	C-2
C-2	Saturn-IB Local and Forebody-Dependent Command Module Loads at $\alpha = 0^\circ$	C-3
C-3	Saturn-IB Local Normal Force Derivatives at $\alpha = 0^\circ$	C-4
C-3	Saturn-IB Local Normal Force Derivatives at $\alpha = 0^\circ$ (Cont.)	C-5
C-4	Saturn-IB Induced Normal Force Derivatives at $\alpha = 0^\circ$	C-6
C-5	Saturn-IB Lumped Load Centers of Pressure at $\alpha = 0^\circ$	C-7
C-6	Saturn-IB Local and Induced Command Module and Flare Axial Force Moment Derivatives at $\alpha = 0^\circ$	C-9
C-7	Saturn-IB Separated-Flow Velocity Ratios at $\alpha = 0^\circ$	C-10
D-1	Saturn-V, Definition of Lumped Normal Force Vectors	D-2
D-2	Saturn-V Local and Forebody-Dependent Command Module Loadings	D-3
D-3	Saturn-V Local Normal Force Derivatives at $\alpha = 0^\circ$	D-4
D-3	Saturn-V Local Normal Force Derivatives at $\alpha = 0^\circ$ (Cont.)	D-5
D-3	Saturn-V Local Normal Force Derivatives at $\alpha = 0^\circ$ (Cont.)	D-6
D-4	Saturn-V Induced Normal Force Derivatives at $\alpha = 0^\circ$	D-7
D-5	Saturn-V Local and Induced Command-Module and Flare Axial Force Moment Derivatives at $\alpha = 0^\circ$	D-8
D-6	Saturn-V Lumped Load Centers of Pressure at $\alpha = 0^\circ$	D-9
D-7	Saturn-V Separated-Flow Velocity Ratios at $\alpha = 0^\circ$	D-11

## Section 1

### INTRODUCTION

Many of the current boosters being considered for manned space-flight missions in the near future are long, flexible vehicles with aerodynamic characteristics that are dominated by separated flow in the transonic Mach number regime. Large, highly non-linear aerodynamic loads that occur in the high-dynamic-pressure region of the trajectory are characteristic of flow separation. For an elastic vehicle, the designer must consider the possibility of structural-aerodynamic coupling that could cause failure of the structure. The Saturn-Apollo family of manned booster vehicles dramatically illustrates the effects of flow separation on elastic vehicles.

Both the Saturn-IB and Saturn-V vehicles have alternating regions of attached and separated flow, as shown in Fig. 1-1. No theoretical method exists for computing the unsteady effects of flow separation. However, a quasi-steady analysis technique for the computation of the aerodynamic damping of such vehicles, using the static load distributions as an input, has been developed. This technique has been used successfully to predict the damping of the Saturn I-Apollo vehicle (Ref. 1). Because of this success, the NASA Marshall Space Flight Center has retained the Lockheed Missiles & Space Company, in a consultant capacity, to apply the quasi-steady analysis technique to the Saturn -IB and Saturn-V boosters.

The quasi-steady analysis may be divided into two steps: (1) preparation of the quasi-steady aerodynamic input, i. e., defining the portions of each loading that are dependent on local and upstream conditions; and (2) application of the resulting aerodynamic loadings to the equations of motion for an elastic vehicle. The derivation of this analytical technique is thoroughly discussed in Ref. 1 and will not be reiterated. Rather, an attempt will be made to describe the effects of structural-aerodynamic coupling in terms of the underlying physical concepts.

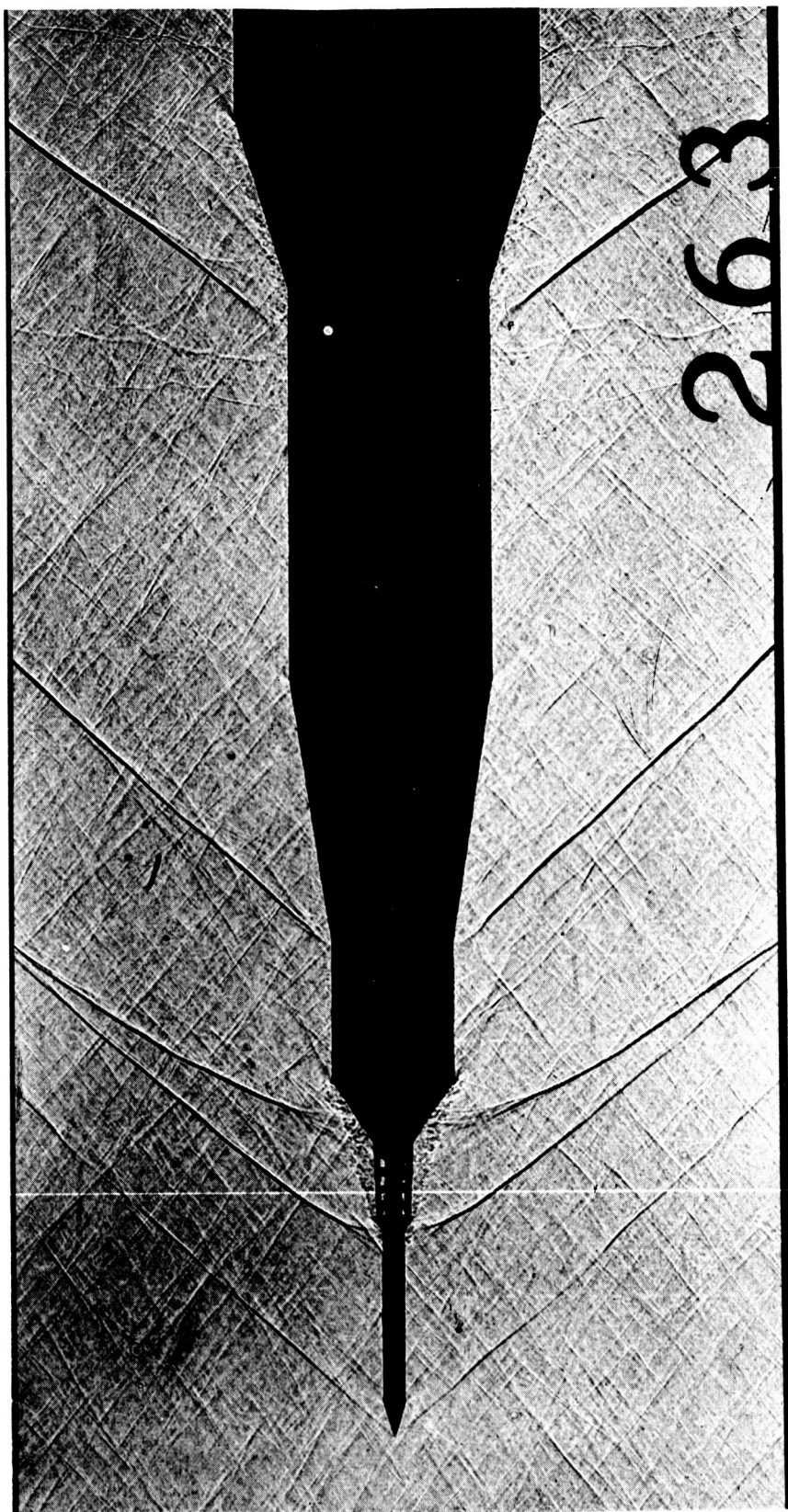


Fig. 1-1 Saturn-V Flow Field at  $M = 1.46$

## Section 2

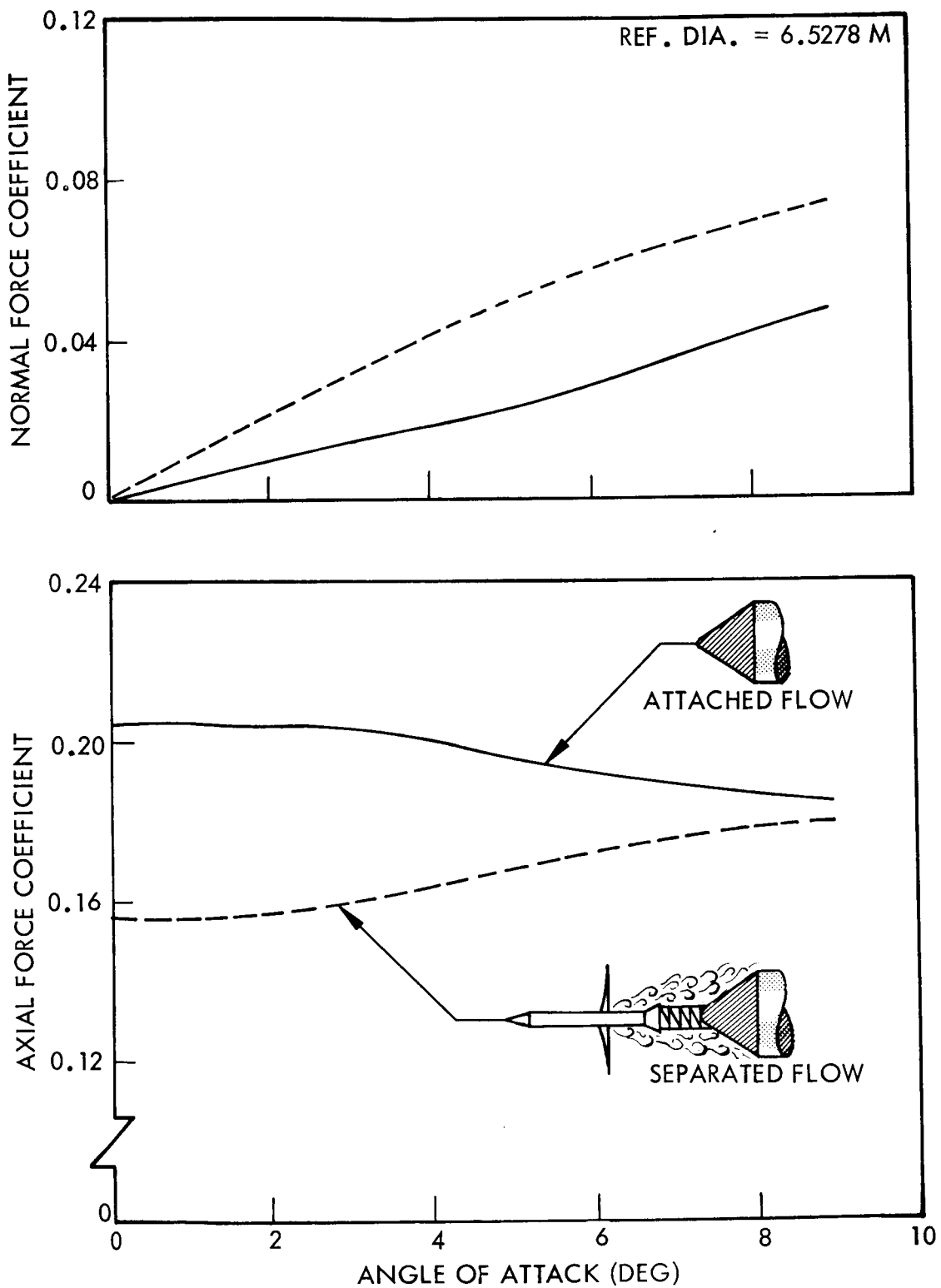
### MECHANICS OF SEPARATED FLOW

The difficulty in predicting the dynamic effects of flow separation arises from the fact that the major separated-flow loading on a submerged body element is the result of conditions upstream of the element at the separation source. By examining the shadowgraph of Fig. 1-1, one may see that the separated-flow field over the command module is generated upstream at the escape rocket. Likewise, the flare separations originate on the preceding cylinders at the shock locations. A time lag will, therefore, exist between the instant a perturbation of the flow field occurs at the separation source and the time the resulting flow-field change has been transmitted to the submerged body, through the separated region, thereby changing its loading. It is this time lag which may cause a phase shift between the static and dynamic effects of separation.

The forebody-induced loading is of major importance in determining the response of a body submerged in separated flow. This loading is deduced from an analysis of the static load distribution. The static load distribution also yields the force dependent on local attitude and supplies the information needed to subdivide the induced load as a function of forebody displacement and forebody attitude. The derivation of the various steady and quasi-steady aerodynamic derivatives is discussed in detail in Ref. 1. A brief summary of their salient features is given in the following sections.

#### 2.1 SEPARATED-FLOW AERODYNAMICS

When extracting the forebody and local crossflow-dependent derivatives from the static data, the concept of a velocity deficit is used. The data shown in Fig. 2-1 indicate that, at  $\alpha = 0^\circ$ , there is an increase in the normal force derivative and a

Fig. 2-1 Command-Module, Attached and Separated-Flow Loads at  $M = 1.0$

reduction in the forebody axial force of the submerged body. The reduced axial force is a measure of the reduced average dynamic pressure within the wake, which can be expressed as

$$\frac{\bar{q}_s}{q_\infty} = \frac{\left( C_{A_0} \right)_s}{\left( C_{A_0} \right)_a} \quad (2.1)$$

where  $s$  refers to separated flow and  $a$  refers to attached flow.

The local attitude derivative  $C_{N_{\alpha_s}}$  may be estimated from the attached flow derivative  $C_{N_{\alpha_a}}$  by the following relation

$$C_{N_{\alpha_s}} = C_{N_{\alpha_a}} \frac{\bar{q}_s}{q_\infty} \quad (2.2)$$

The remainder of the submerged-body load is an induced load expressed by

$$\Delta^i C_{N_\alpha} = C_{N_{\alpha_T}} - C_{N_{\alpha_s}}$$

where  $\Delta^i C_{N_\alpha}$  is the induced derivative and  $C_{N_{\alpha_T}}$  is the measured total derivative.

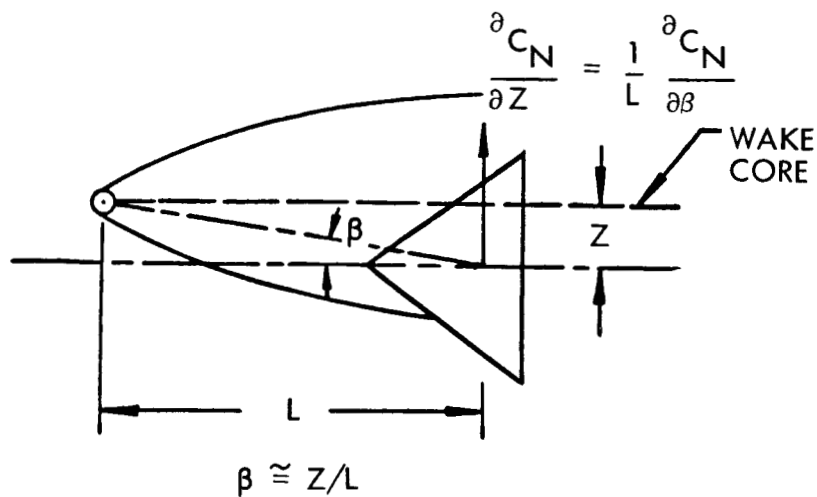
From Fig. 2-2, it is evident that the induced load on the command module ( $\Delta^i C_{N_\alpha}$ ) has two components. One component is a function of the relative displacement angle  $\beta = Z/L$ , while the other is a function of the escape rocket attitude  $\theta_N$ . Thus, we may write the induced load as

$$\Delta^i C_{N_\alpha} = \Delta^i C_{N_\beta} + \Delta^i C_{N_{\theta_N}} \quad (2.3)$$

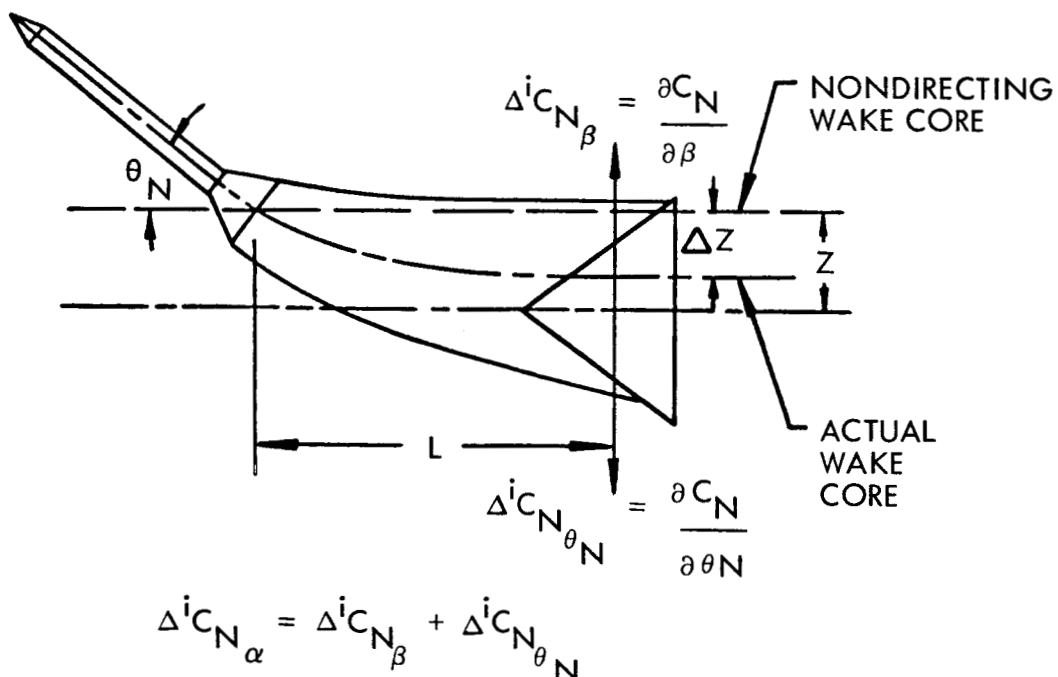
For regions of shock-induced separation, the induced load on the submerged frustum is a function of forebody crossflow only, i.e.,  $\Delta^i C_{N_\alpha} = \Delta^i C_{N_\theta}$  and  $\Delta^i C_{N_\beta} = 0$ .

This may be seen by examining Fig. 2-3. Crossflow over the attached flow portion of the cylinder ( $w = U_\infty \alpha_{ac}$ , which is effectively lumped at the attached flow center of pressure  $x_{ac}$ ) causes the windward boundary layer to thin and the leeward boundary layer to thicken (Fig. 2-3a). This action produces the differential shock locations on the cylinder, since the shock location relative to the frustum is a direct function of the boundary-layer thickness at separation (Ref. 2). Thus, crossflow boundary-layer effects produce a negative cylinder load ( $\Delta^i C_{N_c}$ ) at the shock location and a positive flare load at the reattachment zone ( $\Delta^i C_{N_1}$ ). The remainder of the induced frustum load is caused by crossflow at the shocks ( $\alpha_c$ ). This crossflow changes the relative windward and leeward shock strengths (Fig. 2-3b) and produces the induced derivative  $\Delta^i C_{N_2}$ .

The boundary-layer thickening phenomenon discussed above is illustrated by the shadow-graphs in Fig. 2-4. Two identical configurations were tested, with and without a boundary-layer trip, under the same conditions. In both cases, the boundary layer is turbulent. The trip serves to thicken the boundary layer, causing a forward movement of the separation point as shown.

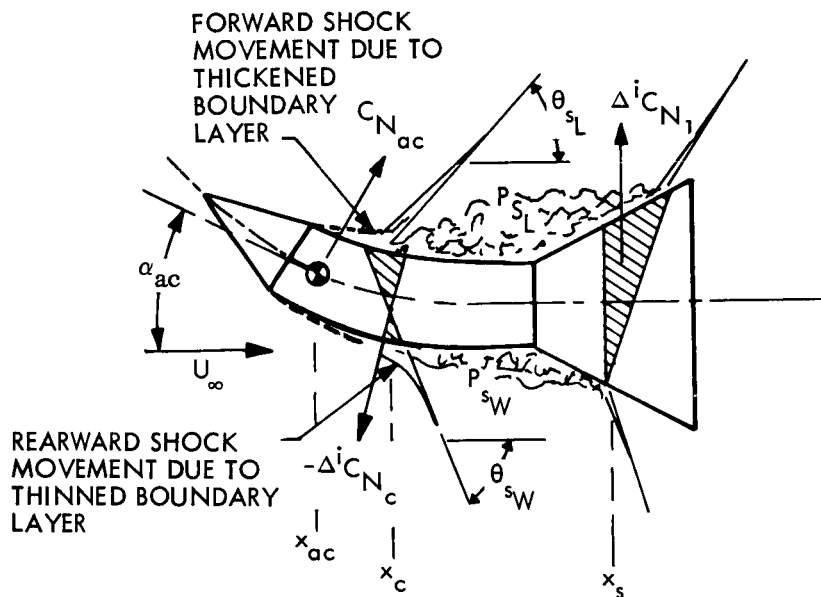


a. Nondirecting Wake Source



b. Directing Wake Source

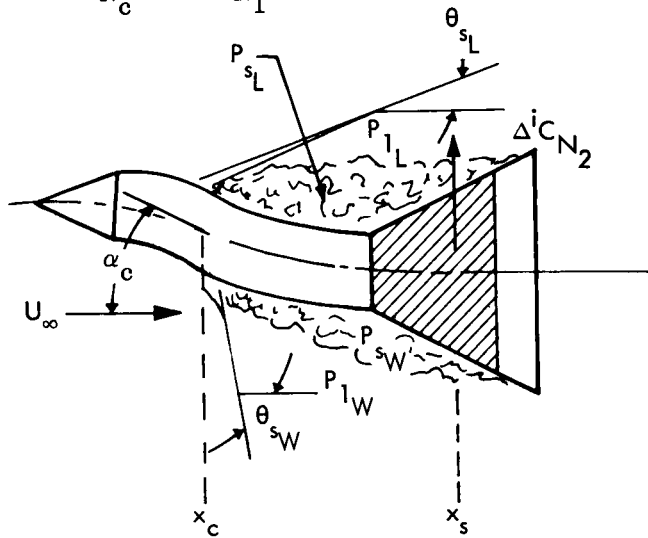
Fig. 2-2 Comparison of Nondirecting and Directing Wake-Source Configurations



$$\theta_{sL} = \theta_{sW} \text{ AND } P_{sL} = P_{sW}$$

a. Effect of Crossflow Forward of Shocks

( $\Delta^i C_{N_c}$  and  $\Delta^i C_{N_1}$  Due to Differential Shock Position)



$$\theta_{sL} < \theta_{sW} \text{ THEREFORE } P_{1L} < P_{1W} \text{ AND } P_{sL} < P_{sW} \text{ SINCE } P_{1L} = P_{sL} \text{ AND } P_{1W} = P_{sW}$$

b. Effect of Crossflow at Shock Location

( $\Delta^i C_{N_2}$  Due to Differential Shock Strengths)

Fig. 2-3 Shock-Induced Loads

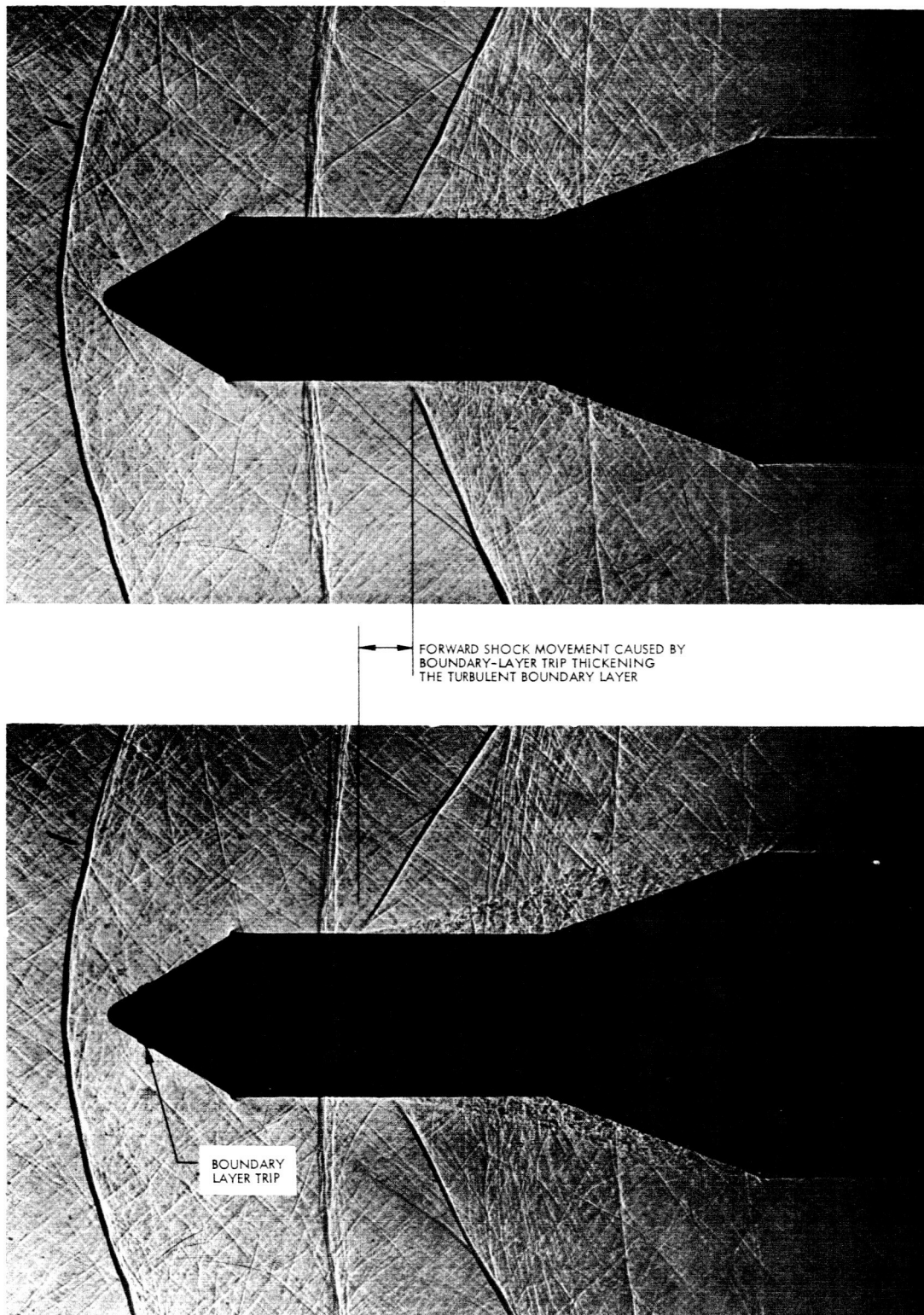


Fig. 2-4 Effect of Boundary-Layer Thickening on Shock Position

## 2.2 QUASI-STEADY LOADS

Quasi-steady loads are static loads modified for slow variations from the static condition. This modification incorporates time dependence into the expression for the loads, as illustrated in Fig. 2-5a. At time  $t$ , the wake-source deflection is  $Z(t)$ ; however, the load applied to the submerged body at this time was generated at an earlier time,  $t - \Delta t$ . The wake-source deflection at time  $t - \Delta t$  was  $Z(t - \Delta t)$ . Thus, the quasi-steady force, which is dependent on forebody displacement, is expressed as

$$\Delta^i C_N(Z)_{QS} = \frac{\partial C_N}{\partial Z} Z(t - \Delta t) \quad (2.4)$$

where

$$\frac{\partial C_N}{\partial Z} = \frac{1}{L} \Delta^i C_{N_\beta} \quad \text{and} \quad \Delta t = L/\bar{U}$$

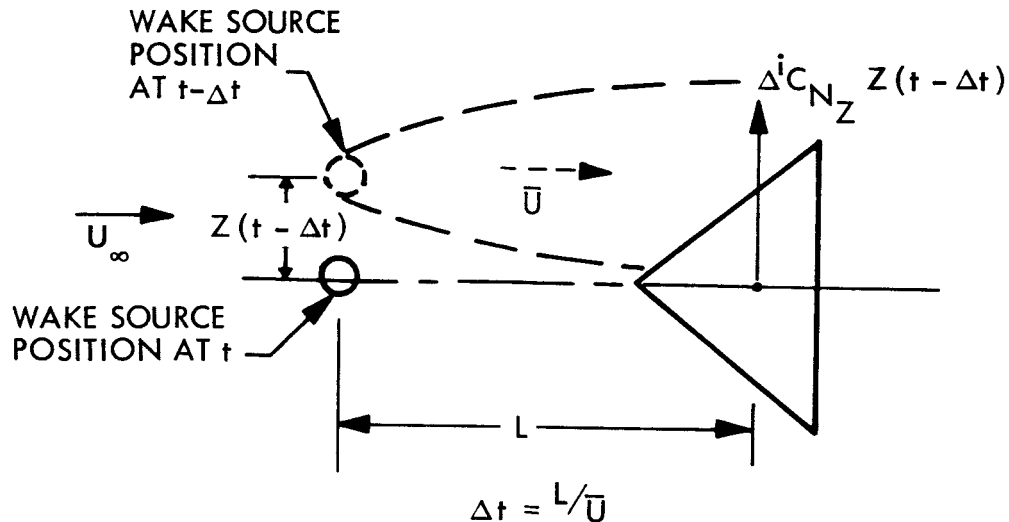
Likewise, Fig. 2-5b shows that the quasi-steady force dependent on forebody attitude is

$$\Delta^i C_N(\theta_N)_{QS} = \frac{\partial C_N}{\partial \theta_N} \theta_N(t - \Delta t) \quad (2.5)$$

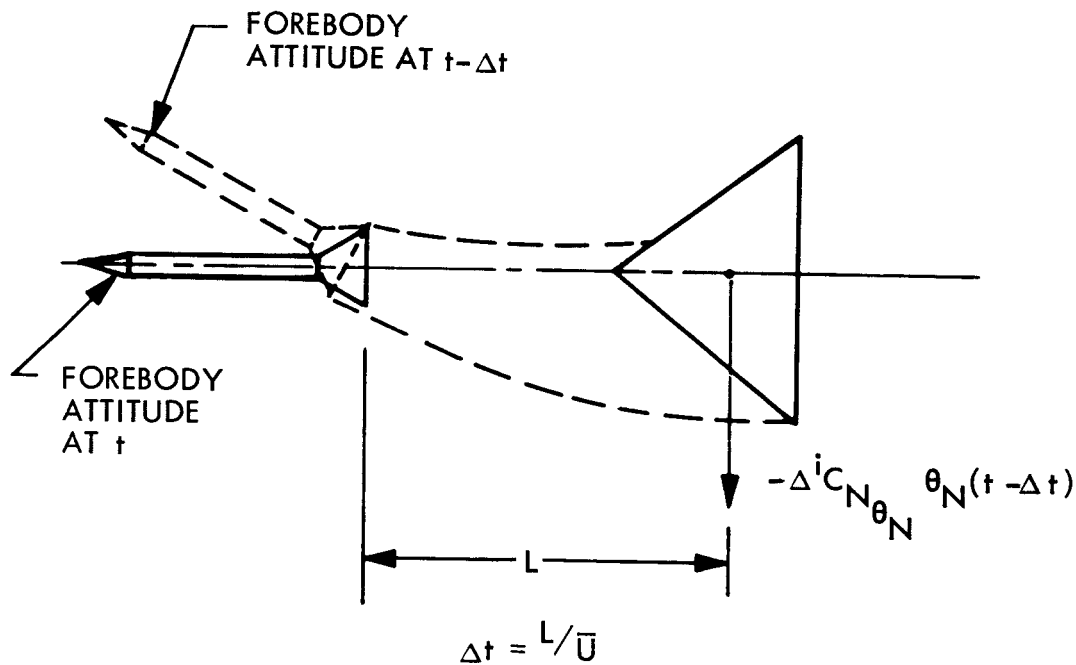
The quasi-steady force dependent on local attitude is

$$C_N(\alpha_s)_{QS} = \frac{\partial C_{N_s}}{\partial \alpha} \left[ \theta(t) + \frac{\dot{Z}(t)}{U_\infty} \right] \quad (2.6)$$

where  $\theta$  and  $\dot{Z}$  are the local attitude and the translatory velocity of the submerged body.



a. Nondirecting Wake Source



b. Directing Wake Source

Fig. 2-5 Quasi-Steady Wake-Source Flow Models

The total quasi-steady load on the command module is the sum of the three loads described by Eqs. (2.4), (2.5), and (2.6).

The average velocity  $\bar{U}$  in the expression for the time lag ( $\Delta t = L/\bar{U}$ ) is derived from the dynamic pressure ratio

$$\frac{\bar{U}}{U_{\infty}} = \left( \frac{\bar{q}_s}{q_{\infty}} \right)^{1/2} = \left[ \frac{\left( C_{A_0} \right)_s}{\left( C_{A_0} \right)_a} \right]^{1/2} \quad (2.7)$$

The quasi-steady, shock-induced load is made up of two components, one dependent upon the crossflow on the cylinder forward of the shocks and the other dependent upon the crossflow at the shock location (Fig. 2-6). These loads may be expressed as

$$\Delta^i C_N(\theta_1)_{QS} = C_{N_{\theta_1}} \alpha_{ac} (t - \Delta t_1 - \Delta t_2) \quad (2.8)$$

and

$$\Delta^i C_N(\theta_2)_{QS} = C_{N_{\theta_2}} \alpha_c (t - \Delta t_2) \quad (2.9)$$

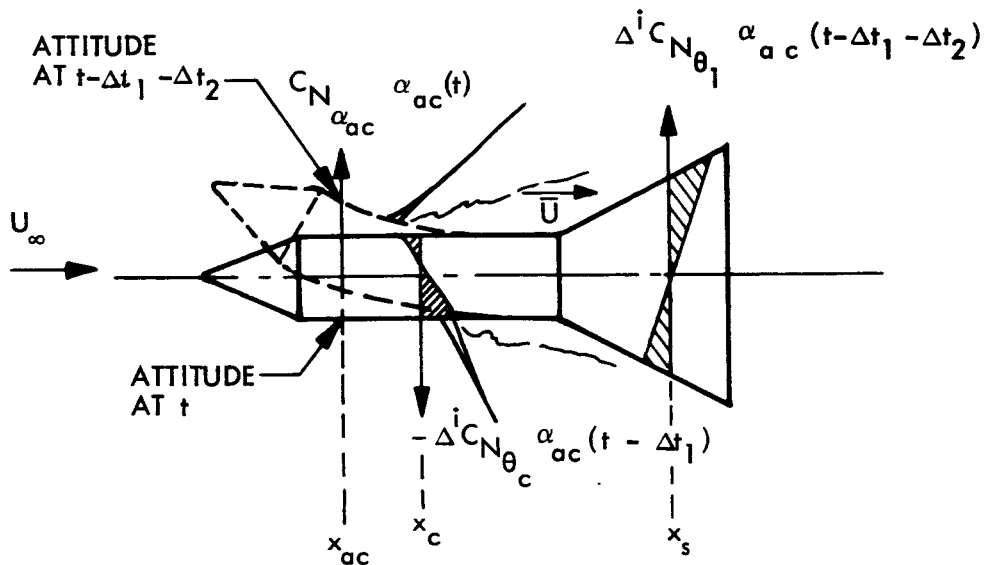
where

$$\Delta t_1 = \frac{x_{ac} - x_c}{0.8 U_{\infty}}$$

[ $0.8 U_{\infty}$  is the convection velocity in a turbulent boundary layer (Ref. 3)]

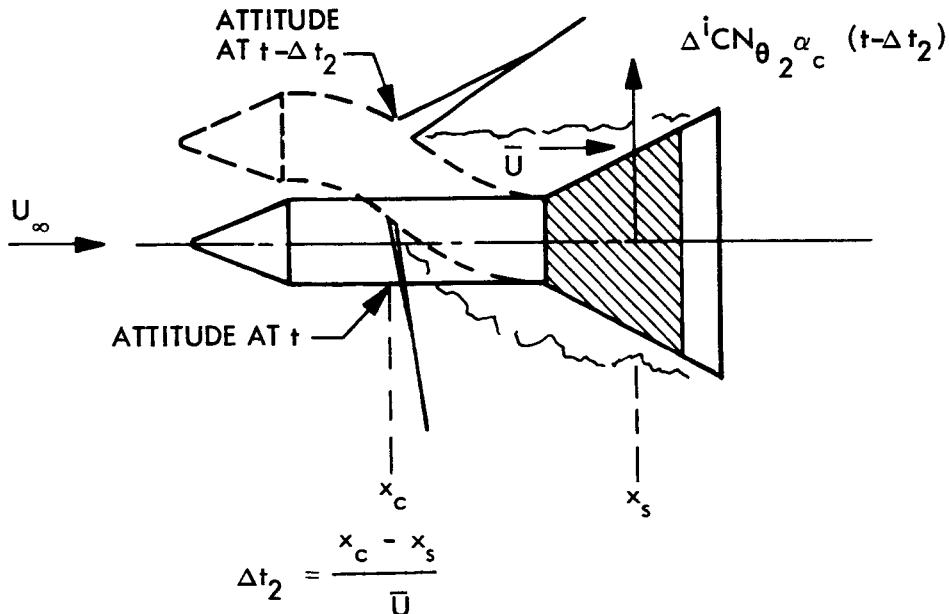
$$\Delta t_2 = \frac{x_c - x_s}{\bar{U}}$$

[ $\bar{U}$  is obtained from the axial force ratio on the flare, Eq. (2.7).]



$$\Delta t_1 = \frac{x_{ac} - x_c}{0.8 U_\infty} \quad \Delta t_2 = \frac{x_c - x_s}{\bar{U}}$$

a. Effect of Crossflow Forward of Shock Location



b. Effect of Crossflow at Shock Location

Fig. 2-6 Quasi-Steady Shock-Induced Separation Flow Model

### Section 3

#### SATURN-APOLLO ANALYSIS

The computation of the aerodynamic damping for the Saturn-IB and Saturn-V booster vehicles was performed applying the quasi-steady analysis technique described in Ref. 1. Figure 3-1, which is taken from Ref. 1, illustrates the degree of agreement obtained between data computed by this method and the experimental data (Ref. 4) for an early Saturn-I configuration.\* The quasi-steady predictions vary slightly (well within the scatter of the experimental data) from those presented in Ref. 1. This is due to a more accurate representation of the command module center of pressure, as discussed later.

The static load distributions over the Saturn-IB and Saturn-V vehicles were obtained through the analysis of all pertinent, currently available data (Refs. 5 through 27). The distributions were reduced to lumped-force derivatives and partitioned into local and induced components. These data are documented for  $\alpha = 0^\circ$  in Appendices C and D for the Saturn-IB and Saturn-V vehicles, respectively. The velocity ratios used in the time lag computations are also included in the appendices. These data were then applied to the equations of motion for the elastic vehicle. A single-degree-of-freedom analysis was performed using the  $t = 60$  sec bending-mode shapes of the Saturn-IB and the Saturn-V vehicles (Refs. 28 and 29).\*\* The analysis was performed for the Mach number range of  $0.8 \leq M \leq 2.0$ , i.e., for the high-dynamic-pressure portion of the vehicle trajectories (Refs. 30 and 31). The results of the analysis are discussed in the following paragraphs.

---

\*The quasi-steady technique assumes that the vehicle oscillates with its natural free-free bending frequency. Results obtained for the first mode of the Saturn-IB [using a nominal value of 1 percent of critical for the structural damping coefficient (Ref. 28)] indicate a maximum deviation from the natural frequency of 2.5 percent.

\*\*Results obtained on the Saturn-V vehicle using the  $t = 80$  sec mode shapes indicate a maximum deviation of 5 percent from the damping value computed using the  $t = 60$  sec mode shapes.

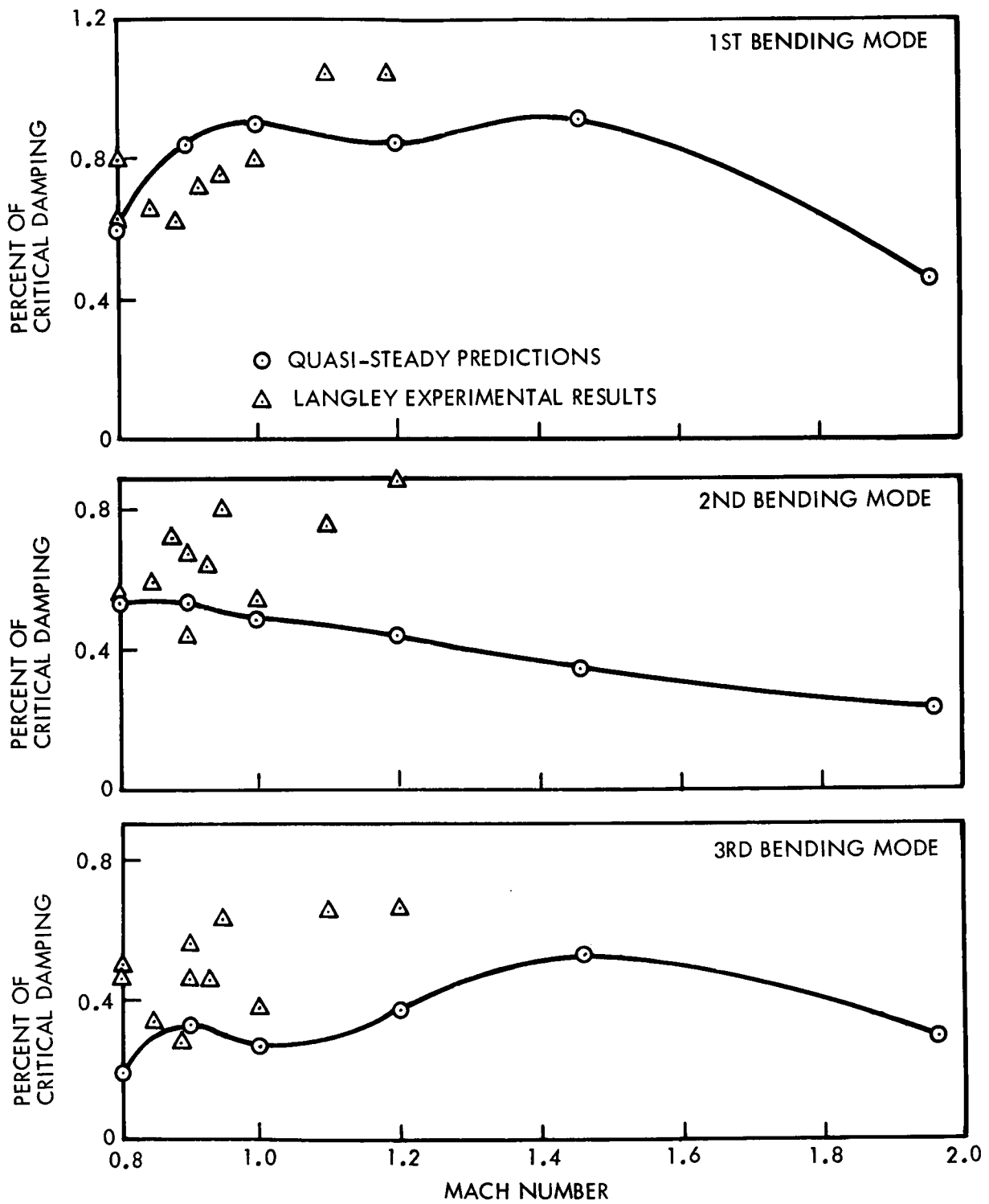


Fig. 3-1 Aerodynamic Damping at  $\alpha = 0^\circ$  of the Saturn I-Apollo Vehicle with Escape Rocket (Disk Off)

### 3.1 STATIC AERODYNAMIC ANALYSIS

Like the Saturn-I vehicle, the Apollo payload is responsible for the major effects of flow separation for both the Saturn-IB and Saturn-V vehicles. The escape-rocket wake represents the most prominent single region of flow separation (Fig. 1-1). Furthermore, the modal deflections and mode slopes are large on the forward portion of the vehicle; and the large separation-induced load on the Apollo payload has a very significant effect on the vehicle damping. The major portion of the analytical and experimental effort was expended in obtaining the loading over the Apollo-payload portion of the vehicles.

The static load distribution, key to the quasi-steady loads, is normally obtained from pressure distribution data. However, when regions of shock-induced separation occur, it is impossible to define the narrow, shock-induced negative loadings from pressure data alone. Therefore, segmented force data (Refs. 5 and 6) were used in conjunction with the pressure data; and the magnitudes of the ill-defined, negative load peaks were varied until agreement with the force data was obtained for both normal force and center of pressure. Figures 3-2 and 3-3 show the type of agreement finally obtained for local body elements. A constant bias exists for the center of pressure location on the interstage frustum between the service module and the S-IVB stage. This bias results from the axial force moment, on the frustum, that is not accounted for in the reduction of the pressure data.

The pressure data used in the analysis of the forebody loads (Ref. 7) were measured on a model that had a rod passing through the tower structure to support the escape rocket. This rod\* is visible in the shadowgraph (Fig. 1-1). Component force data were obtained with and without the rod to determine if the rod restricted the wake movement (Refs. 5, 6, and 8). The data from Figs. 3-2 through 3-4 indicate no wake steering effects. These data do serve, however, to modify the representation of the command module center of pressure (Fig. 3-4) relative to that used on the Saturn-I

---

\*Rod diameter/escape rocket diameter = 0.777.

(Refs. 32 and 33). Excellent agreement between the summed, lumped force distribution for the Saturn-IB and Saturn-V vehicles (Fig. 3-5) and the overall force data is shown in Figs. 3-6 and 3-7, respectively.

### 3.2 AERODYNAMIC DAMPING ANALYSIS

In the quasi-steady analysis technique, an equivalent damping derivative is computed for each lumped force. These damping derivatives are multiplied by  $(-\rho U_\infty S/4\omega \tilde{m})$  to give the local damping contribution as a fraction of critical damping. The sum of these contributions gives the total damping. A damping distribution can be developed from the damping vectors. Like the static load distribution, the damping distribution indicates which loads contribute favorably and unfavorably to the dynamic stability, aeroelastic stability in this case. However, the damping distribution is dependent on Mach number; and it changes with mode shape as the nodes, deflections, and slopes vary. The damping derived through virtual work considerations is directly proportional to the displacement of the local body element.\* Thus, the nose of a bending body has a disproportionately large damping influence, since the relative deflections are usually largest there.

All these factors come into play in the correlation of the damping distribution with the static loads. Figure 3-8 compares the static load and aerodynamic damping distributions for the first three modes of the Saturn IB. The effects of mode-shape changes are striking and become apparent even on the most casual inspection. The effect of relative displacement is manifested by the large contribution from the small escape-rocket-nose load to the damping in all three modes. Detailed consideration of the first-mode damping distribution reveals many of the structural-aerodynamic coupling effects. The large command-module damping is the combined result of the large relative deflection between the escape rocket and command module and the large local deflection at the command module. The damping loads get progressively smaller further aft as the node is approached. The frustum load is partially positive and partially negative, since a node occurs at the frustum. This node location changes the sign of the separation-induced, aft-frustum damping. The same is true for the third

---

\*This relationship holds true for regions of separated flow as well as for attached flow.

mode. The entire frustum load produces damping for the second mode because the relevant node occurs aft of the frustum. Returning to the command module, the damping contributions to the second and third modes are small. Second mode damping is minimized by the opposite effects of deflection and wake steering, and third mode damping is limited because of small mode slopes and relative deflections. Tail barrel damping is small for all modes, because of the small local deflections.

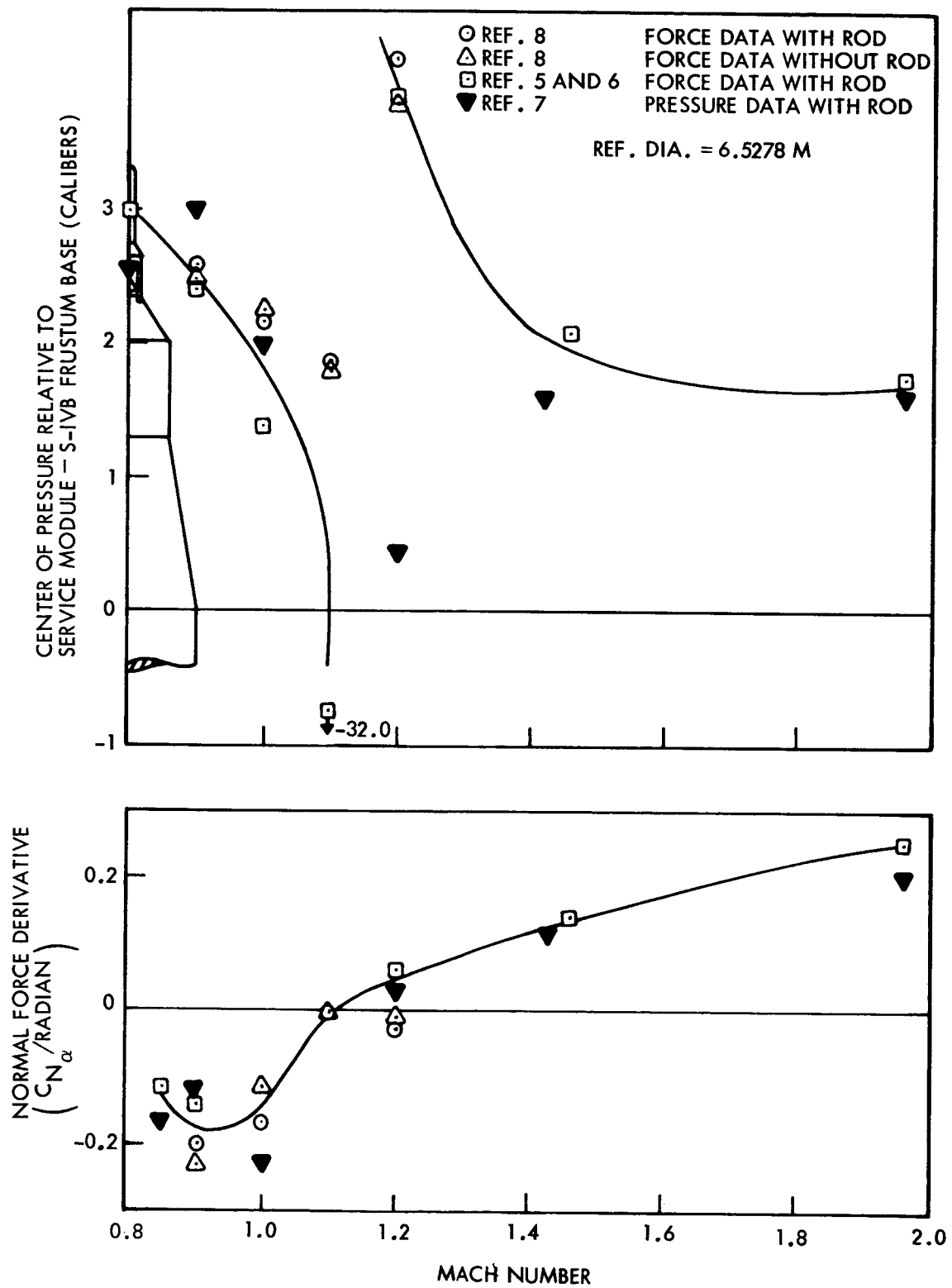
Two representations of the aft S-IVB stage loads are shown in Fig. 3-8. The loading indicated by the phantom line represents the fairing used in Ref. 9, while the solid line represents the data points presented therein. The authors have elected to believe the data points, assuming that they represent the loads in a local separated region caused by terminal normal shocks. The opposite signs of the damping contributions for these two representations reflect the separated-flow interpretation of the latter fairing. In the first and third modes, the total effect of either fairing is about the same, since the loads oppose one another and also are small due to small local deflections. In the second mode, the separated-flow fairing gives appreciable negative damping. The forward negative shock-induced load occurs at a node, producing zero damping, while the positive load occurs aft of the node producing undamping. The resultant damping is, therefore, negative. The results of both representations are shown in Fig. 3-9.

In comparing the Saturn-IB and Saturn-V damping with the Saturn-I results (Fig. 3-9), certain differences in the trends of the data become apparent. They are explained by differences in mode shape and external configuration. For example, at subsonic Mach numbers, the Saturn-IB and Saturn-V vehicles show a sudden increase in their first mode damping relative to the Saturn-I vehicle. Figure 3-10 indicates that this can be explained by the differences in the damping contribution from the interstage frustum between the service module and the S-IVB stage. Figure 3-11 further supports this conclusion. This figure shows that if the cylinder-flare damping were zero, as it is for the Saturn-I, the Saturn-IB and Saturn-V damping would have the same trends as the Saturn-I damping.

For the third mode (Fig. 3-9), a major difference in trend occurs at supersonic Mach numbers. This is entirely due to mode shape differences, since the responsible loads – the command module and shoulder loads – are the same statically for all three configurations. The relatively larger contribution to the Saturn-I damping occurs because of larger modal slopes and deflections at the escape rocket, resulting in larger separation induced damping (Fig. 3-12). The differences in the "noninduced" command module displacement effects between the Saturn I and IB are small due to small local displacements. The Saturn-V damping is nearly zero because of the node location on the command module.

In Figs. 3-13 and 3-14, the damping characteristics of the Saturn-IB and Saturn-V vehicles at 4- and 8-deg angles-of-attack are compared with the damping characteristics at a 0-deg angle-of-attack. There appears to be little change in the overall vehicle damping with angle-of-attack. This is to be expected, since the various opposing positive and negative, separation-induced loads decrease proportionately with increasing angle-of-attack.

In quasi-steady analysis, it has been shown that each separation-induced damping component is related directly to its static counterpart. It is obvious, then, that this technique can be used to discover the cause of any overall vehicle undamping and to suggest possible fixes.

Fig. 3-2 Saturn-IB and Saturn-V Service Module Loads at  $\alpha = 0^\circ$

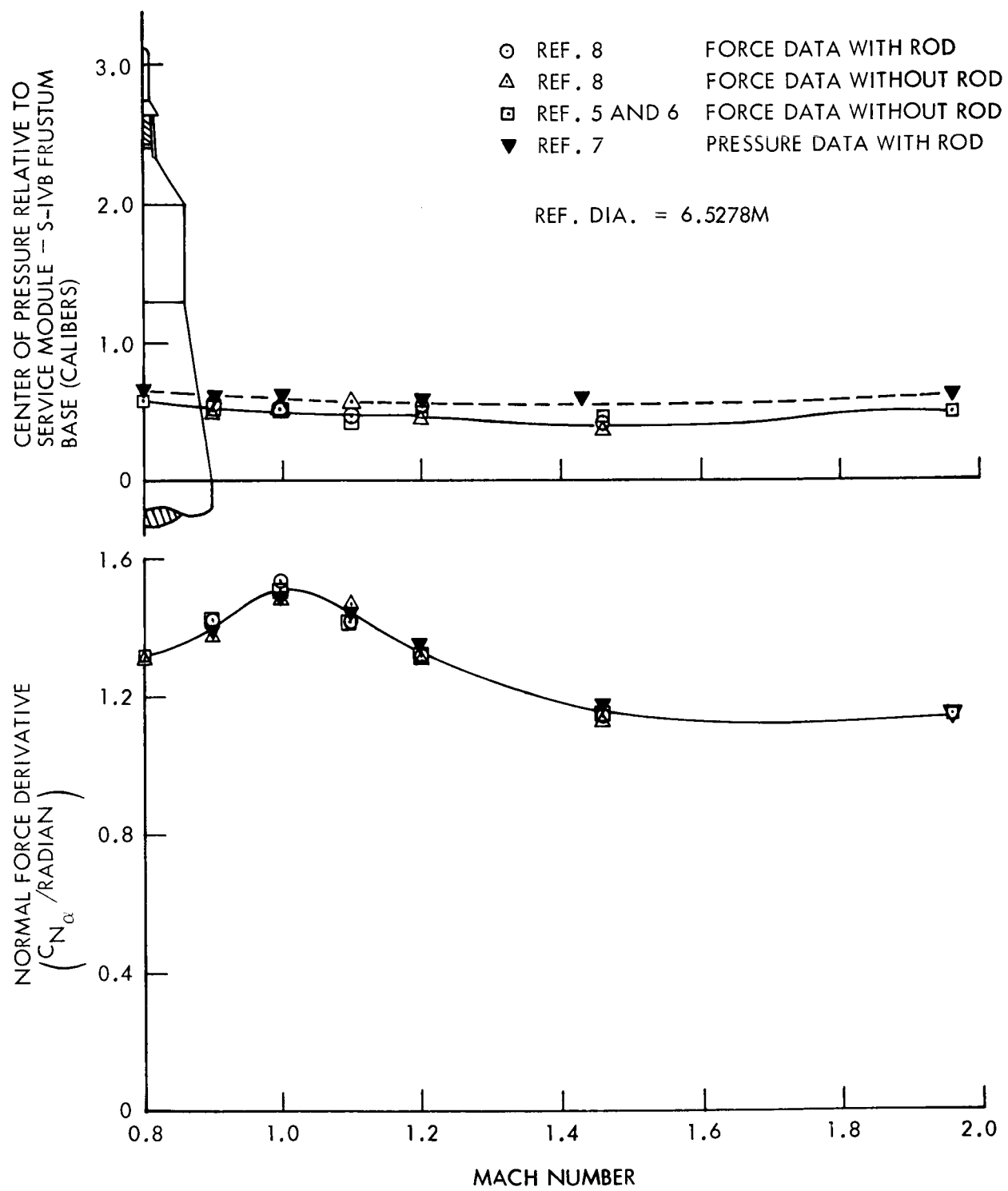
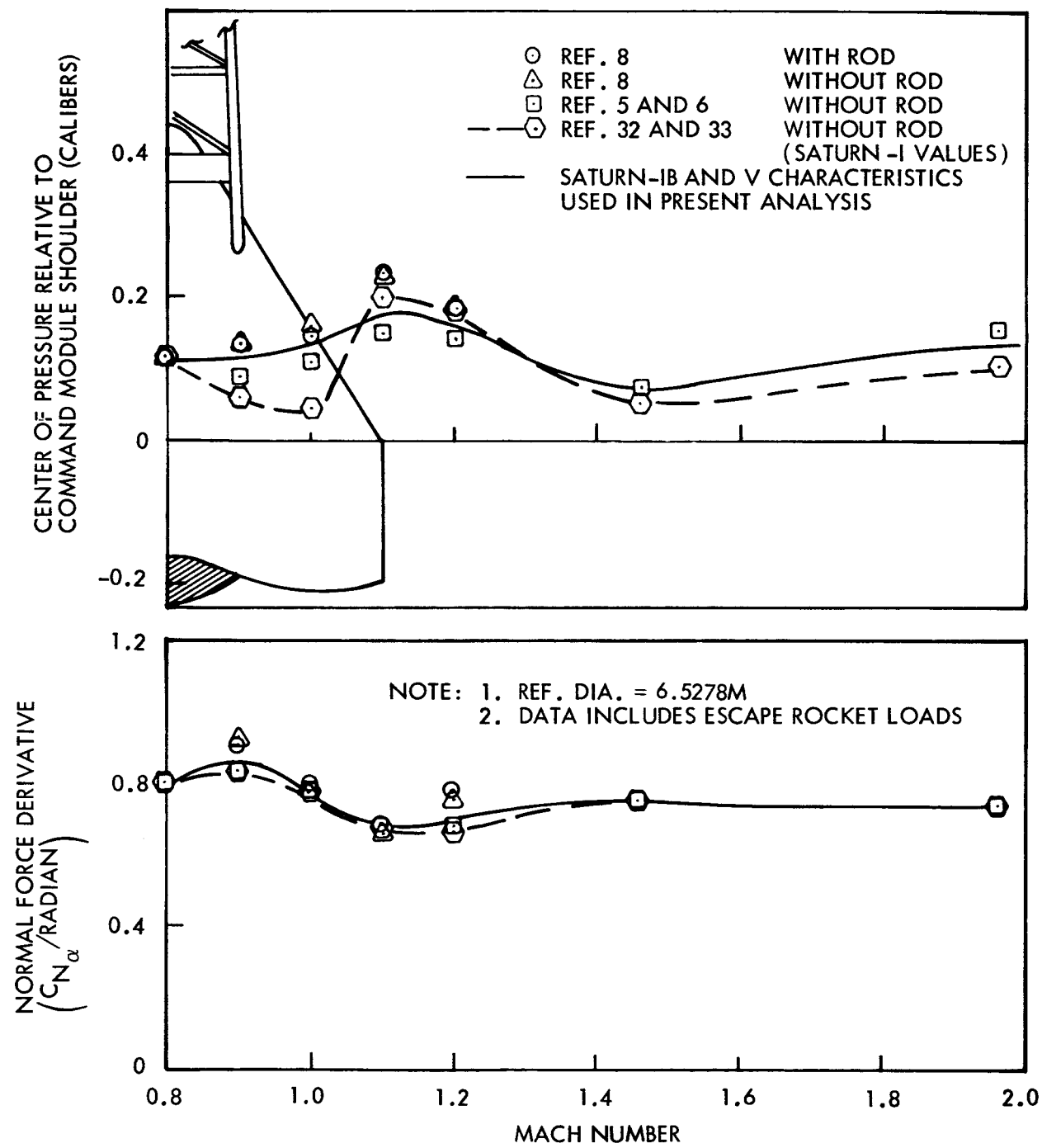


Fig. 3-3 Saturn-IB and Saturn-V Service Module - S-IVB Interstage Frustum Loads at  $\alpha = 0^\circ$

Fig. 3-4 Saturn-IB and Saturn-V Command-Module Loads at  $\alpha = 0^\circ$

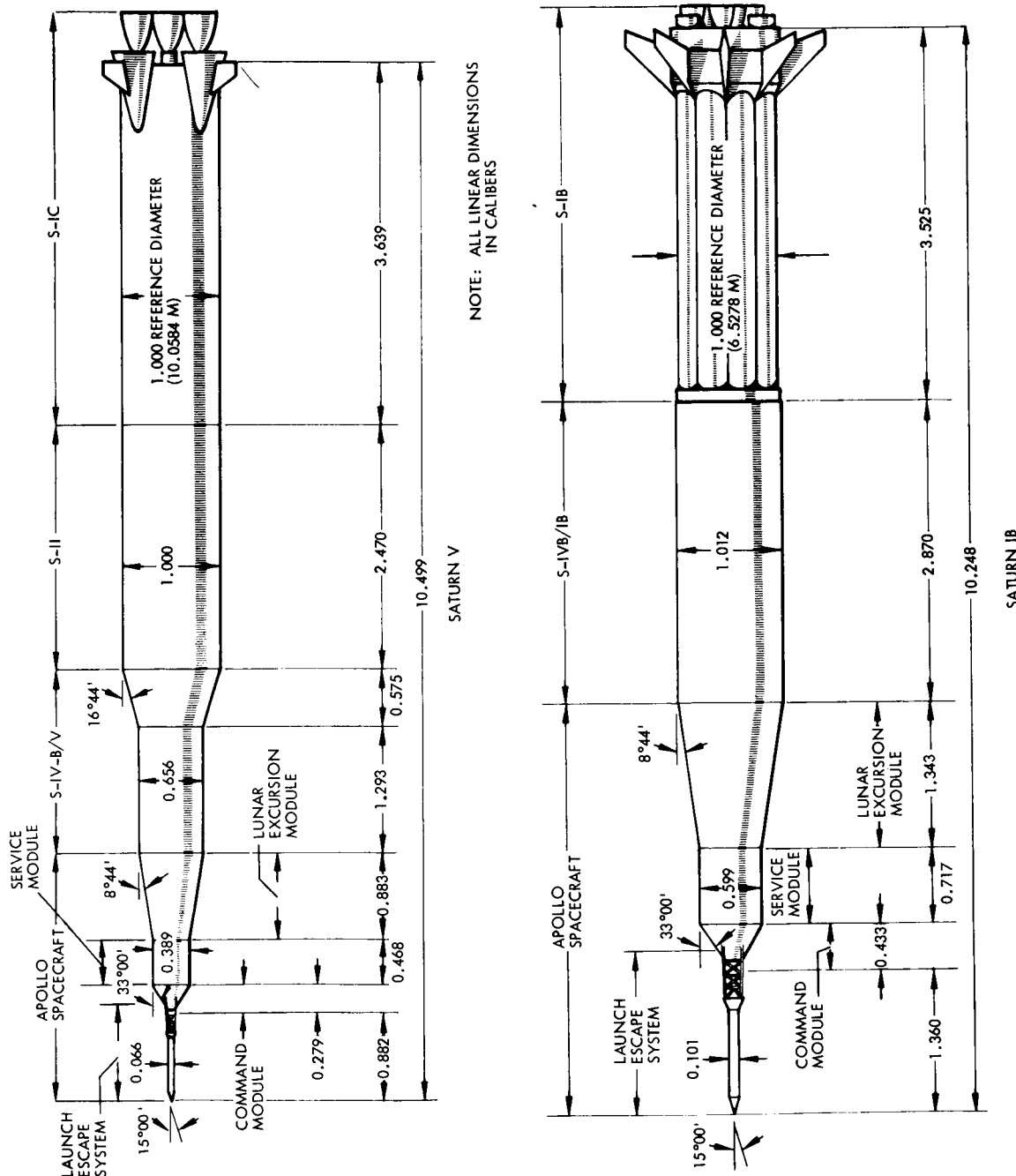


Fig. 3-5 Saturn - Apollo Configurations

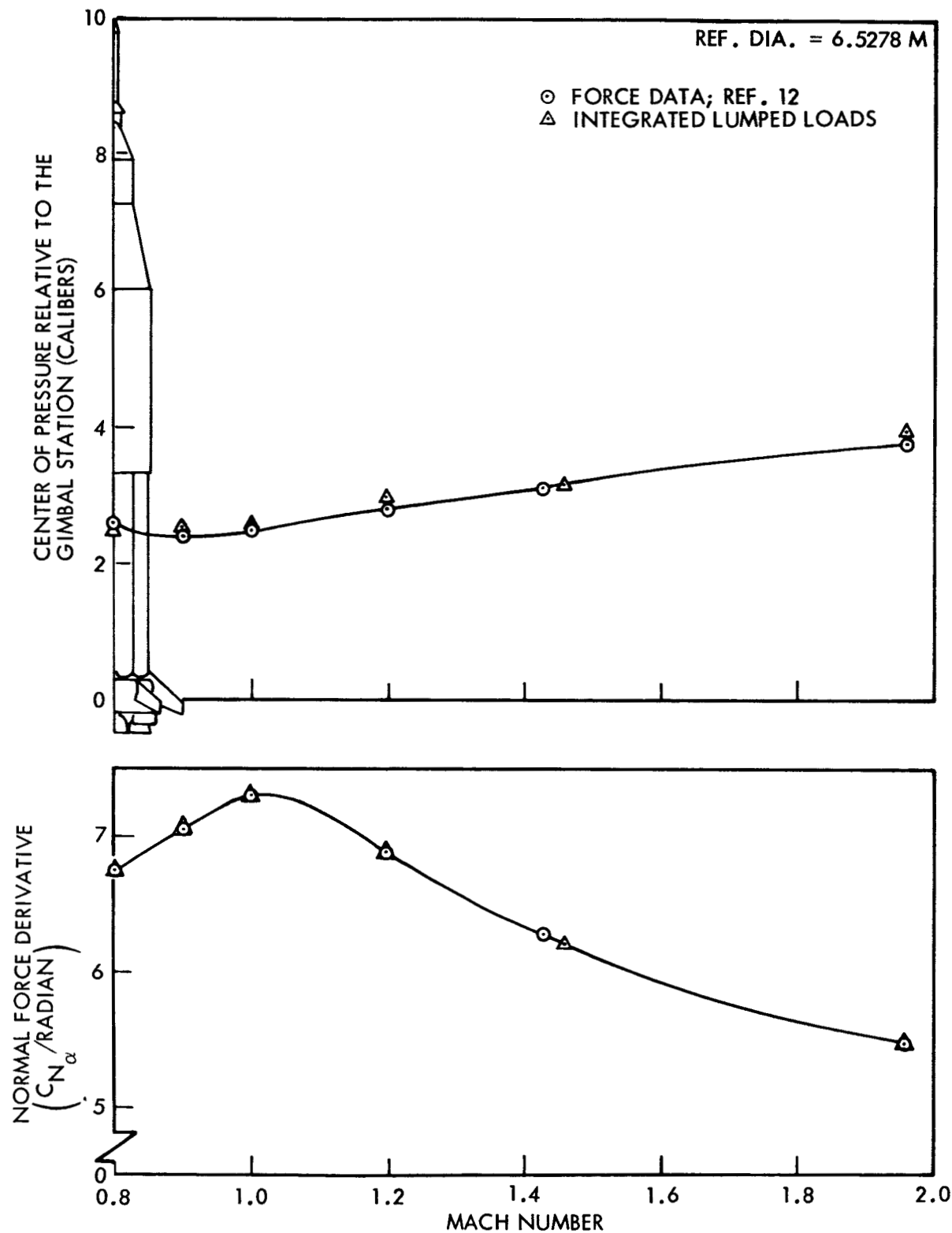


Fig. 3-6 Comparison of Saturn-IB Integrated Lumped Loads with Force Data Results at  $\alpha = 0^\circ$

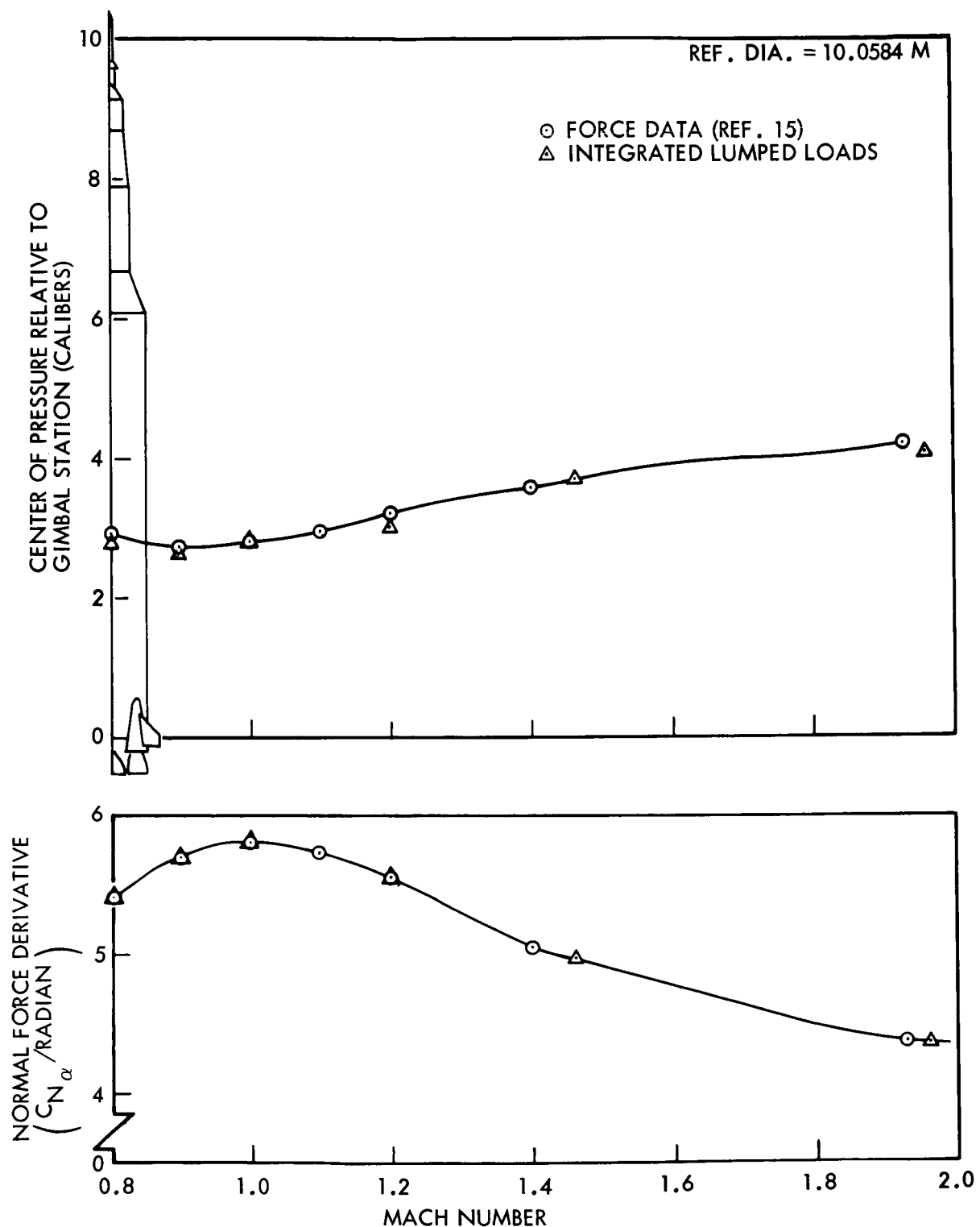


Fig. 3-7 Comparison of Saturn-V Lumped Loads and Force Data  
Results at  $\alpha = 0^\circ$

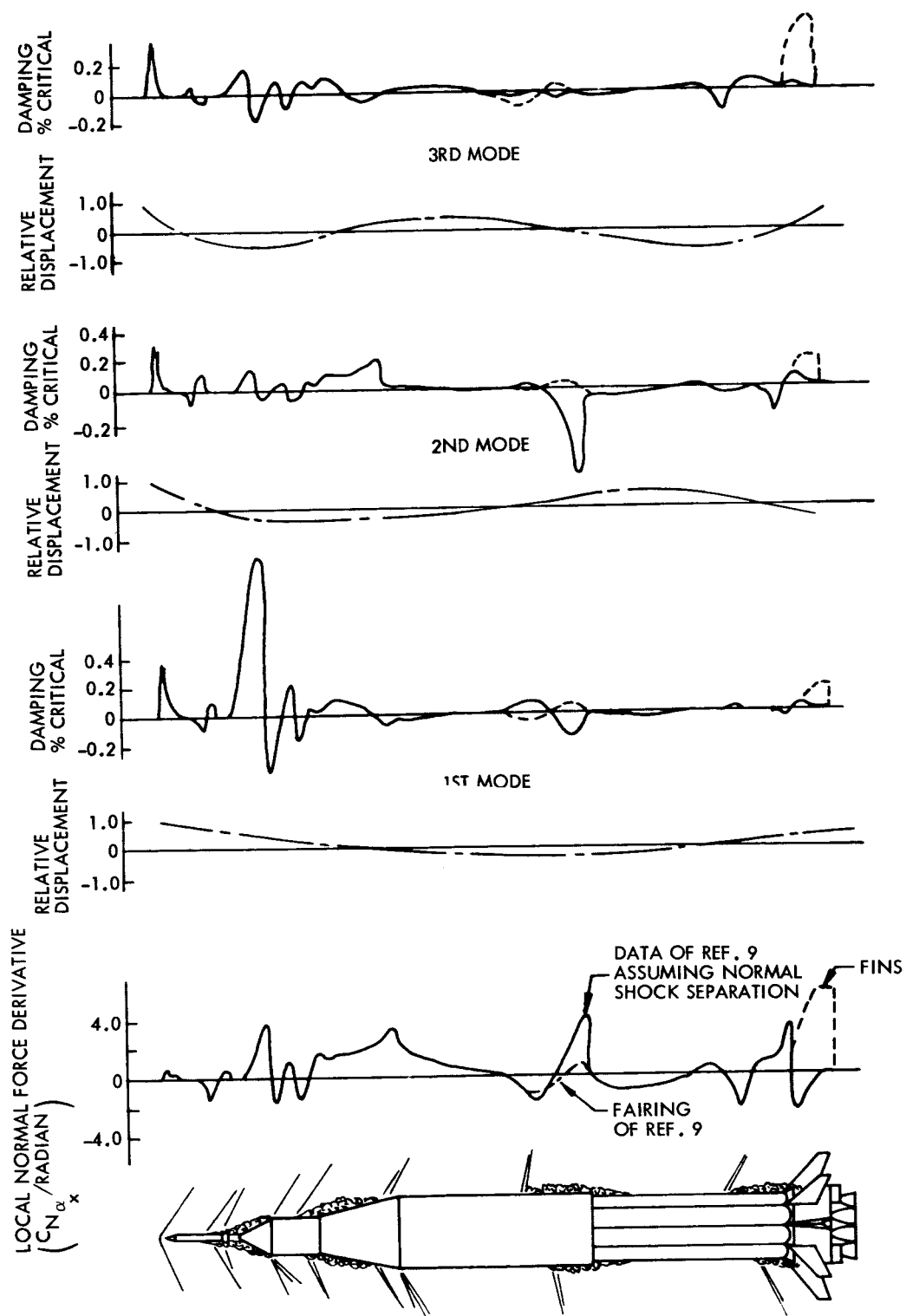


Fig. 3-8 Correlation of Saturn-IB Static and Dynamic Separated-Flow Loads at  $M = 1.2$

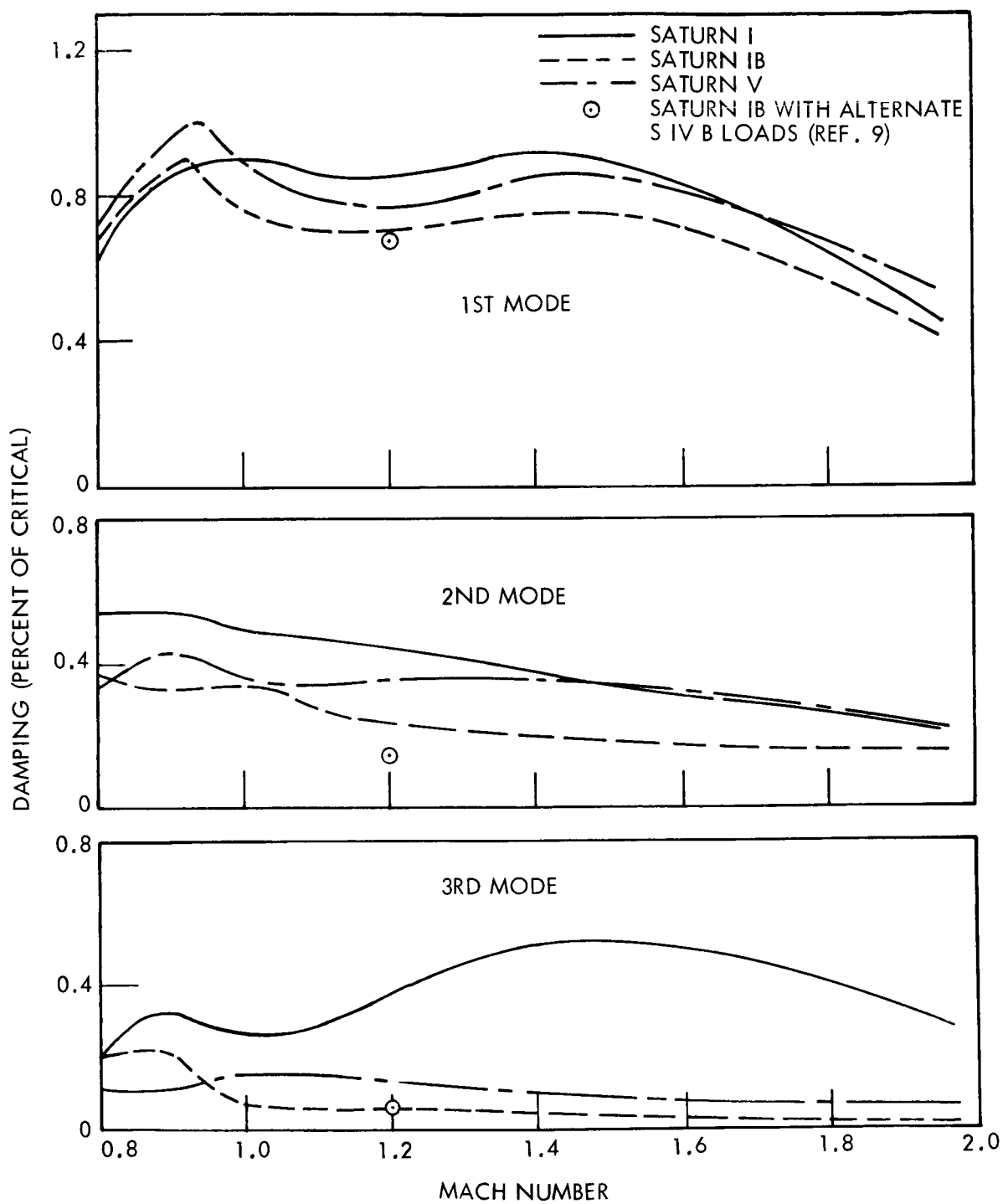


Fig. 3-9 Comparison of Saturn - Apollo Damping Characteristics at  $\alpha = 0^\circ$

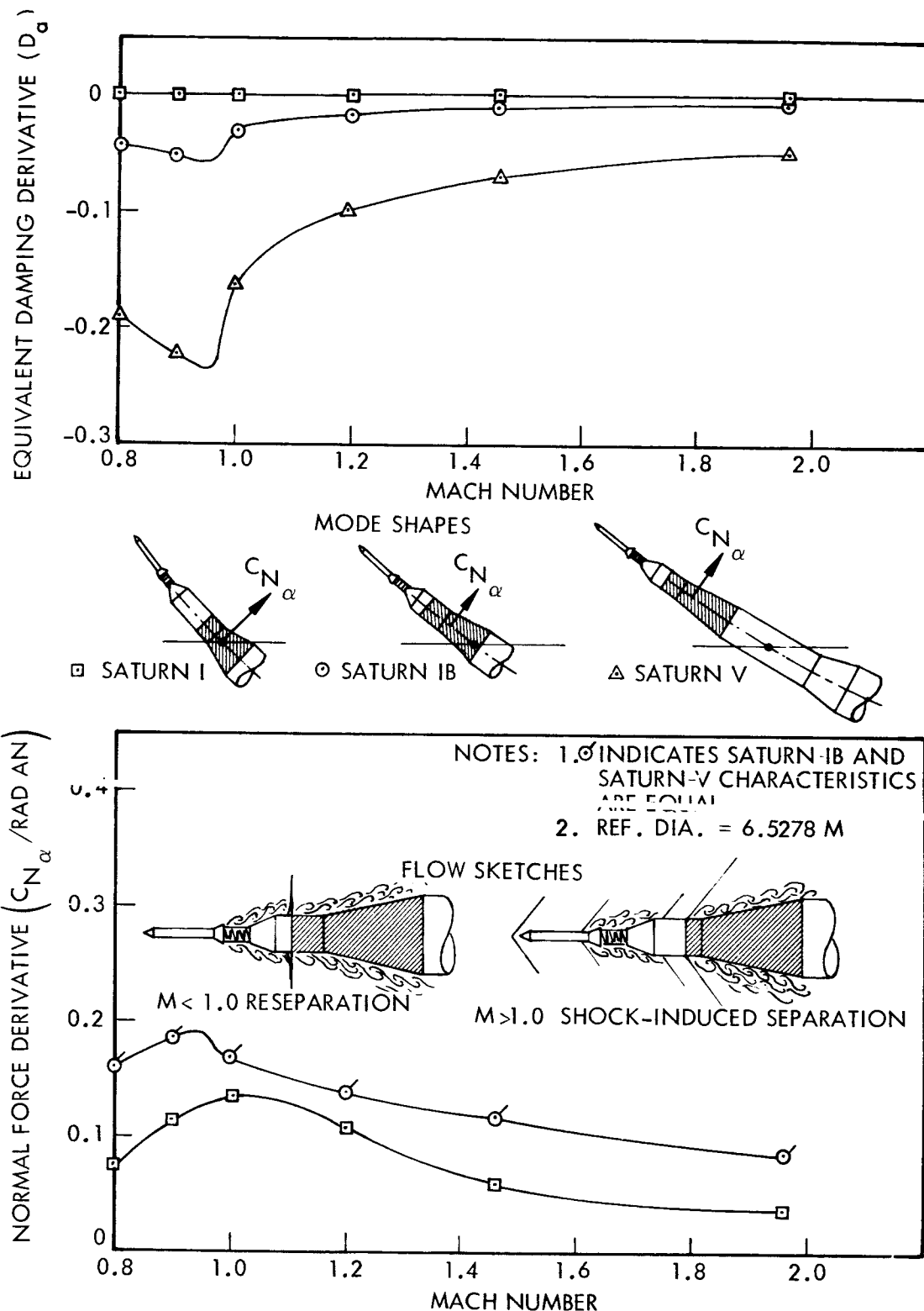


Fig. 3-10 Comparison of Static and Dynamic Characteristics of the Service Module - S-IVB Interstage Loads

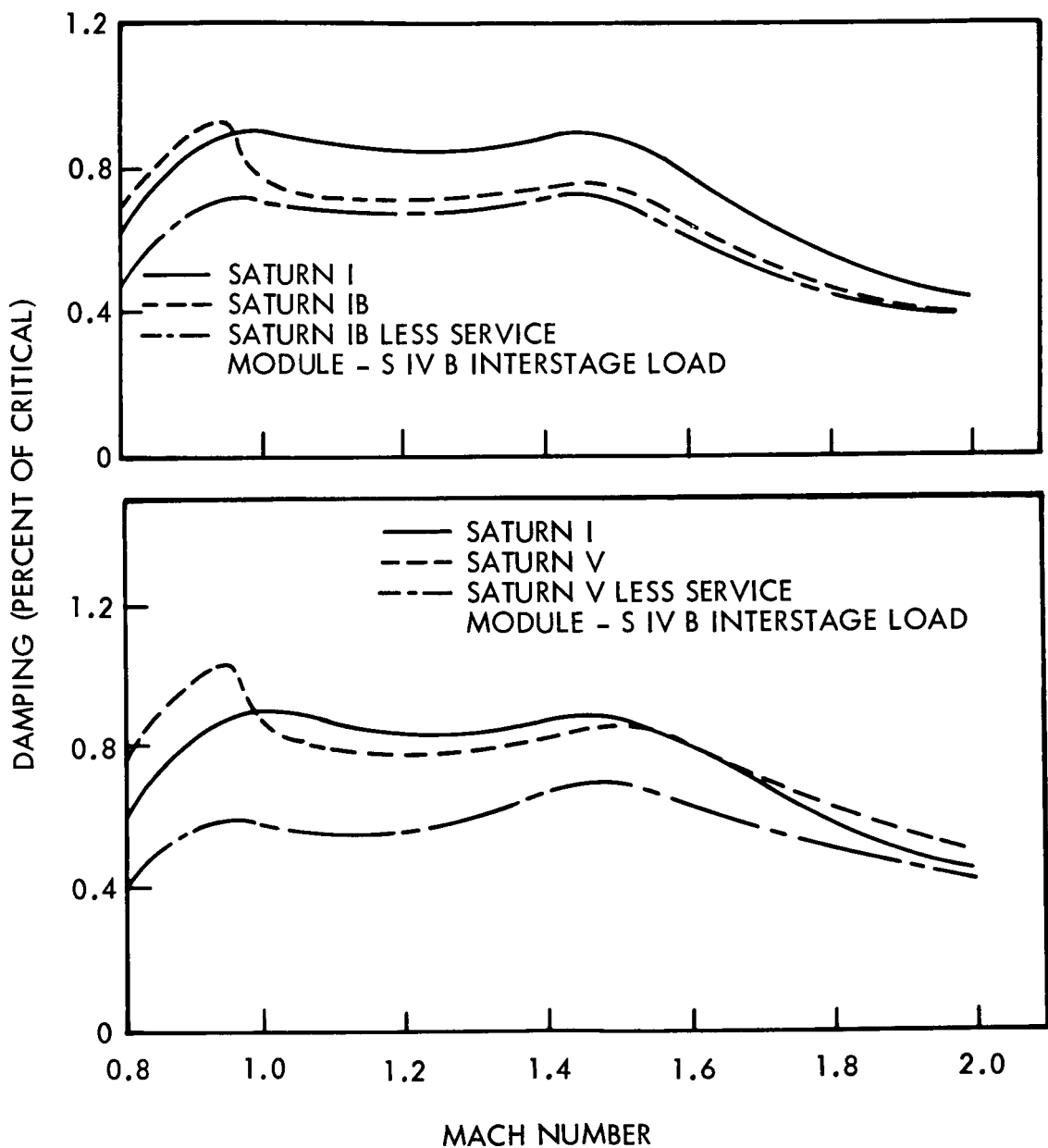


Fig. 3-11 Effects on the Saturn-Apollo 1st Mode Damping of the Service Module - S-IVB Interstage Loads

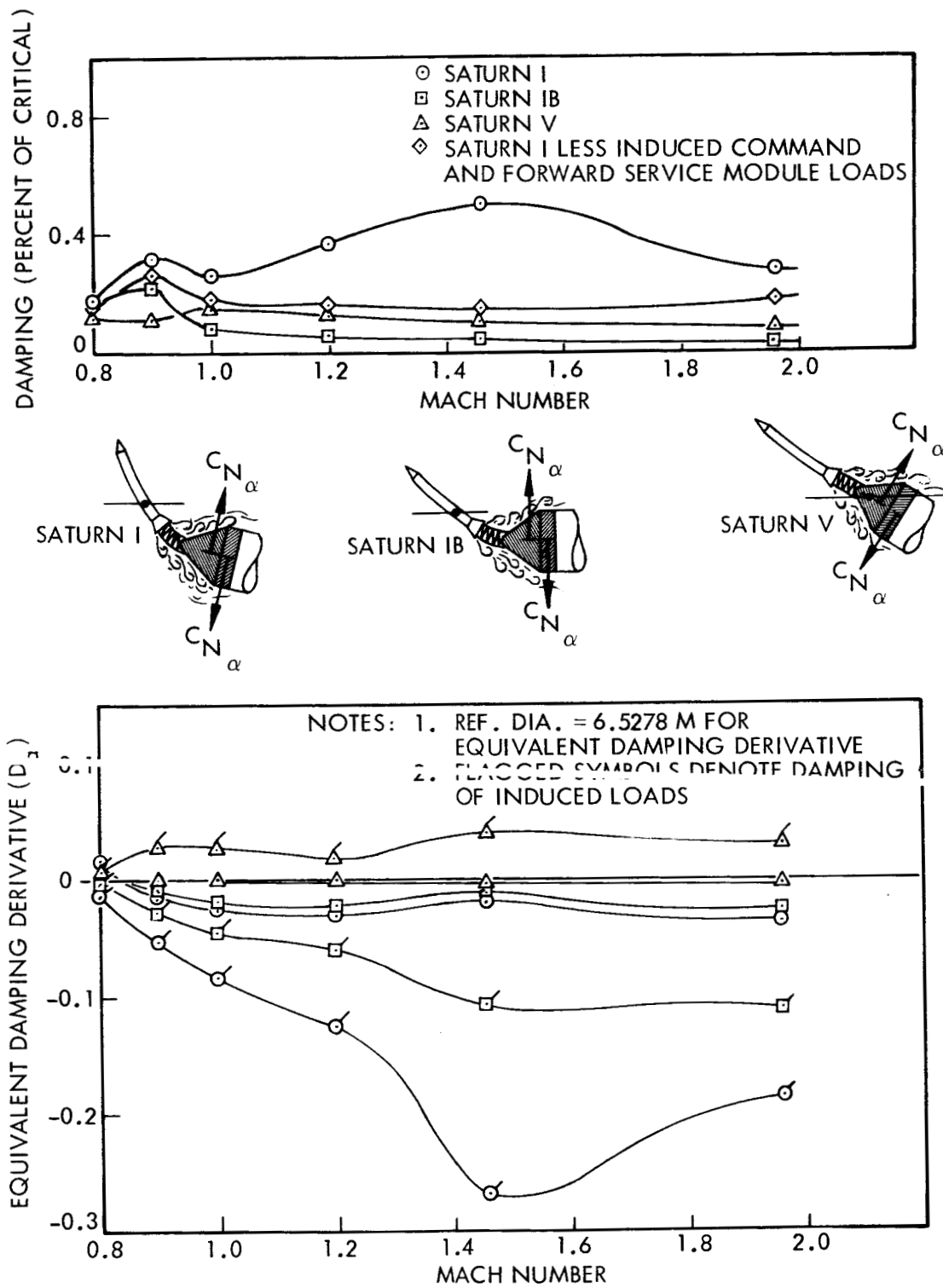


Fig. 3-12 Effects on the Saturn-Apollo 3rd Mode Damping on the Command Module and Forward Service Module Loads

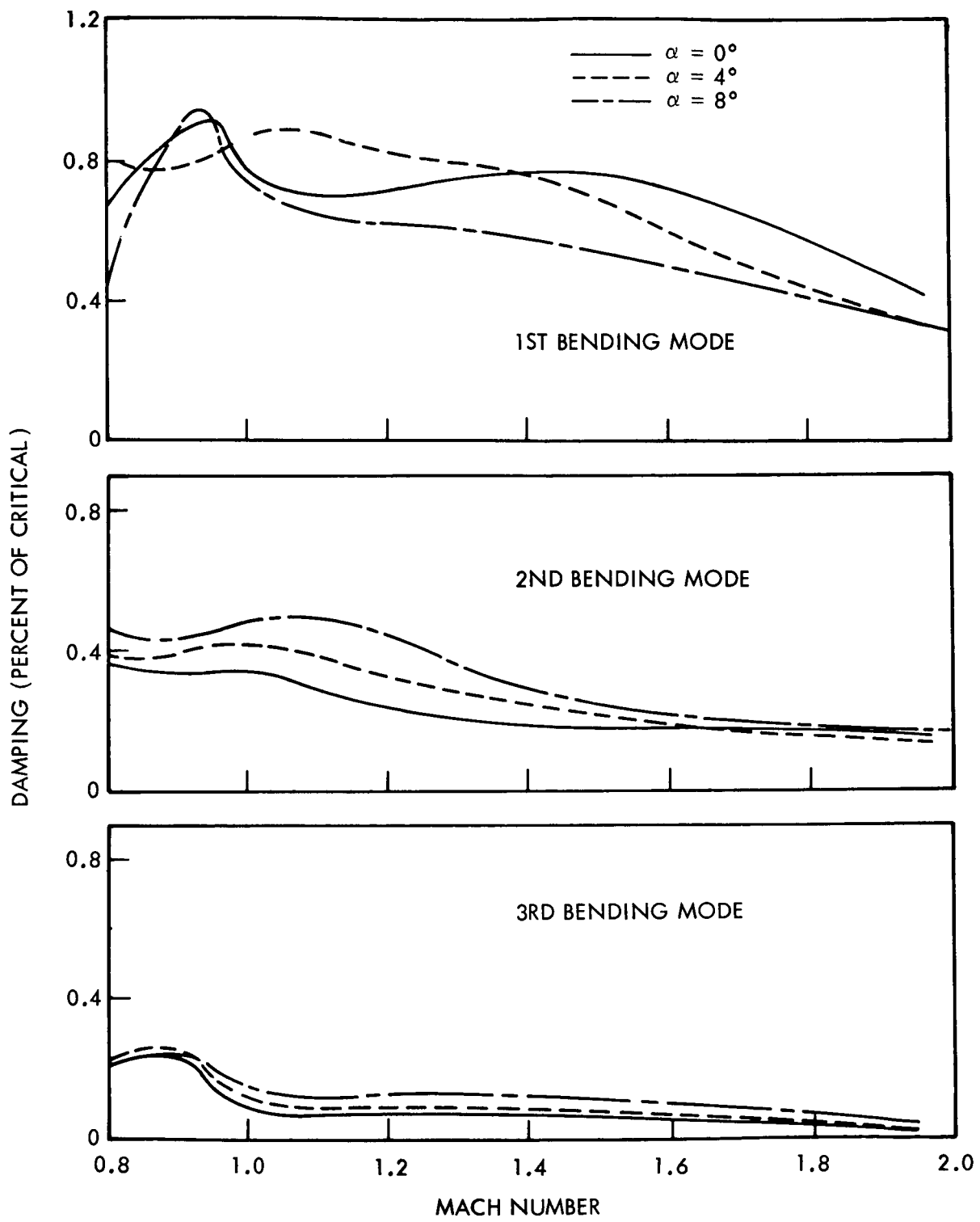


Fig. 3-13 Saturn-IB Aerodynamic Damping

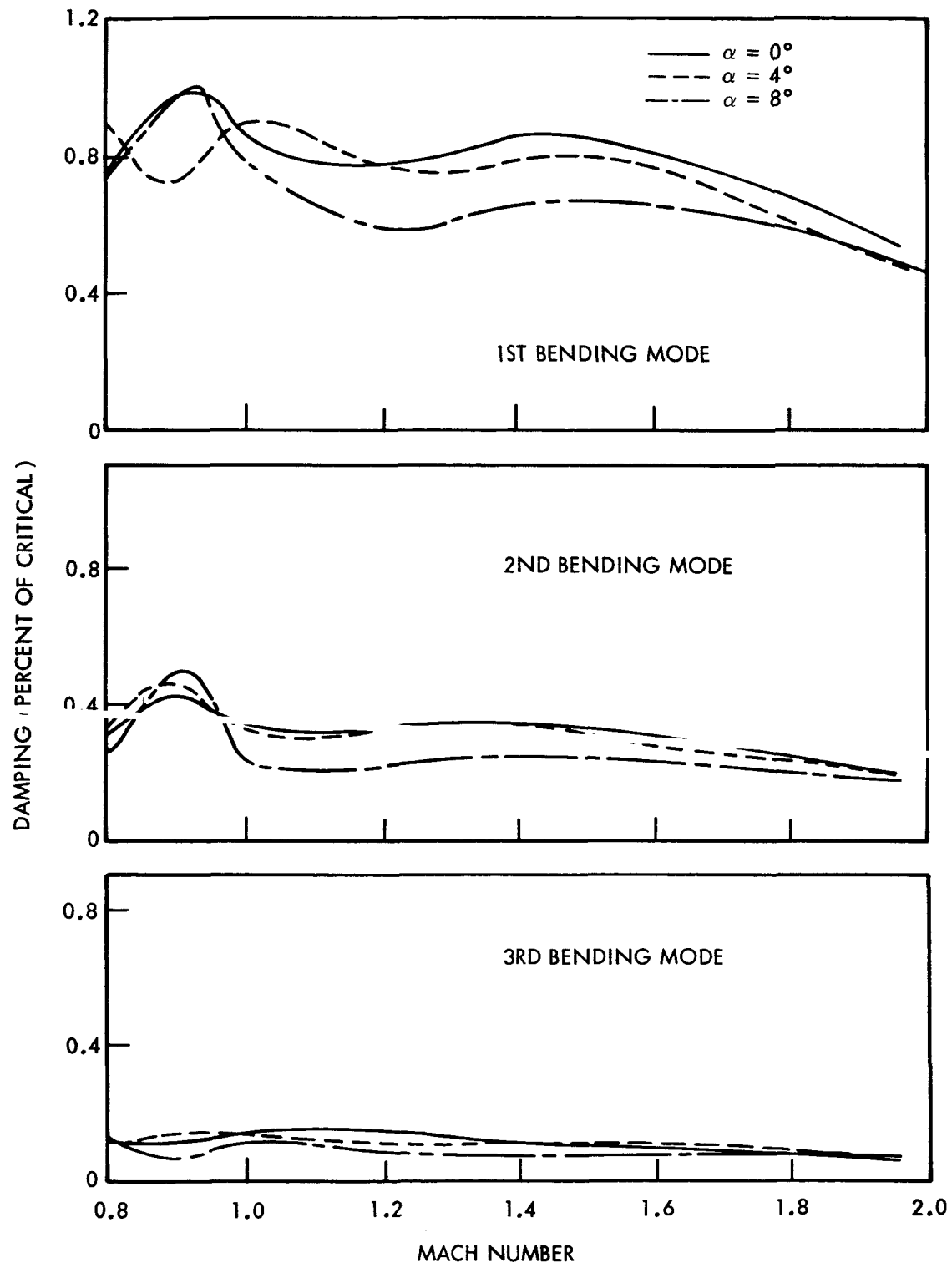


Fig. 3-14 Saturn-V Aerodynamic Damping

Section 4  
CONCLUSIONS

Application of the quasi-steady analysis technique to the Saturn-Apollo launch vehicles, which are aerodynamically dominated by separated flow, has shown that:

- Quasi-steady predictions of the aerodynamic damping for the Saturn-I vehicle agree well with experimental aeroelastic data.
- The damping characteristics of the various Saturn configurations may be correlated using quasi-steady theory.
- In the critical Mach number range ( $0.8 \leq M \leq 2.0$ ), quasi-steady theory predicts that the first three bending modes of the Saturn-IB and Saturn-V vehicles are aerodynamically damped.

It may, therefore, be confidently concluded that both the Saturn-IB and Saturn-V vehicles will have positive aerodynamic damping throughout their atmospheric ascent.

## Section 5

### RECOMMENDATIONS FOR FURTHER STUDY

The flow field over the Saturn-Apollo vehicles is very complex and many of the separation-induced loads still defy rigorous definition. As was indicated in Ref. 1, the analytical partitioning into local and induced components of both the negative shoulder loads and the shock-induced flare loads needs to be improved. This may be facilitated by correlating the quasi-steady results with experimentally determined damping values for simpler wind tunnel model configurations that do not have a multitude of separated-flow regions. Coupled with this work, a basic investigation of the effects of angle-of-attack on shock-induced separation should provide a better and more sophisticated representation of shock-induced unsteady loads.

The above investigations should also shed some light on the effect of flare crossflow and attitude on the shock-induced separation upstream of the flare. A similar upstream effect of the command module on the shock-induced separation at the escape-rocket flare may exist. This effect could be resolved by quasi-steady wake-source tests, somewhat more sophisticated than those proposed in Ref. 1. In addition to driving the wake source harmonically in the pertinent modes of motion and measuring the response of the command module, the command module must also be driven, and the response of the escape rocket must be measured as well as the unsteady forces on the command module.

Finally, further work is needed to make the computer program described in Ref. 1 more reliable and more versatile. Paradoxically, increased reliability can be gained only through sacrifices, however small, in accuracy. By extensive use of curve fitting routines, the amount of input needed can be reduced drastically, leaving less room for the "hard-to-catch" random human error. In order to facilitate fast discovery of the errors that still may slip through, all the input data used in the computations could

be displayed graphically using the General Dynamics/Electronics SC-4020 cathode-ray plotter. (Note: The plots should show the input data as computed by the curve fitting routines, i.e., show the data curves actually used in the computations.) There is a need for built-in options in the computer program that will allow dual (extreme) representations of loads that, for various reasons, are not uniquely defined. This feature will be particularly valuable in the analysis of new, "preliminary design" configurations.

Section 6  
REFERENCES

1. Lockheed Missiles & Space Company, Report on Saturn I – Apollo Unsteady Aerodynamics, by Lars-Eric Ericsson and J. Peter Reding, LMSC A650215, Sunnyvale, Calif., Feb 1964 (U)
2. NASA Ames Research Center, Turbulent Boundary-Layer Separation Induced by Flares on Cylinders at Zero Angle of Attack, by Donald M. Keuhn, NASA TR R-117, Moffett Field, Calif., 1961 (U)
3. Jet Propulsion Laboratory, California Institute of Technology, The Fluctuating Pressure Field in a Supersonic Turbulent Boundary Layer, by A. L. Kistler and W. S. Chin, TR 62-277, Pasadena, Calif., Aug 1962 (U)
4. NASA Langley Research Center, Transmittal of Preliminary Aerodynamic Damping Determined Experimentally from the 8-Percent Apollo/Saturn Aeroelastic Model SD-1, Langley Field, Va. 4 Apr 1963 (C)
5. Brown Engineering Company, Inc., Wind Tunnel Investigation to Determine Transonic Stability Characteristics on a 0.8117 Percent Scale Model of the Saturn IB and V Upper Stages with Several Service Module Lengths and LEM Adapter Angles, by W. Dewayne Radford, Tech Memo AA-8-64-1, Huntsville, Ala, 3 Aug 1964 (U)
6. ----, Wind Tunnel Investigation to Determine Transonic Stability Characteristics on a 0.8117 Percent Scale Model of the Saturn IB and V Upper Stages with Several Service Module Lengths and LEM Adapter Angles; Series II, by W. Dewayne Radford, Tech Memo AA-11-64-9, Huntsville, Ala, 30 Nov 1964 (U)
7. The Boeing Company, Saturn V Upper Stages Pressure Distribution W/APS Units Longitudinal Pressure Distribution and Local Normal Forces for Future Studies in S-II and S-IVB Region of Separation (0.505% Scale), by J. Wright, Project AD-5-63, 6 Apr 1964 (U)

8. NASA Marshall Space Flight Center, Wind Tunnel Investigation to Determine the Effect of an Axial Rod in the LES Tower on the Static Longitudinal Stability Characteristics of the Saturn IB Upper Stage Components, by William C. Pope, Jr., MSFC TN AA-12-64-1, 3 Dec 1964 (U)
9. Chrysler Corporation, Space Division, Static Pressure and Normal Force Co-efficient Distributions on the Saturn IB Launch and Aborted Launch Configurations as Determined by Wind Tunnel Tests, by F. Chianese, Jr., TN-AE-63-12, New Orleans, La, 30 Dec 1963 (U)
10. -----, Results of a Wind Tunnel Investigation to Determine the Pressure and Local Normal Force Distribution Over the Saturn IB Vehicle, by H. B. Reese, TN-AE-63-3, New Orleans, La, 1 Aug 1963 (U)
11. -----, Unpublished Data for Wind Tunnel Tests Described in "Test Plan to Determine the Stability and Axial Force Characteristics of the Saturn IB Launch Vehicle and Components," by F. Chianese, TN-AE-64-61, New Orleans, La, 16 Nov 1964 (U)
12. NASA Marshall Space Flight Center, Static Longitudinal Stability and Axial Force Characteristics of the Saturn IB/Apollo Launch Vehicle as Determined from Tests of a 1.32 Percent Scale Model at Langley Research Center, by J. Johnson, MSFC Memo NR: R-AERO-AD-64-94, Huntsville, Ala, 15 Oct 1964 (U)
13. -----, Experimental Static Longitudinal Stability and Drag Characteristics of the Saturn IB/Apollo Vehicle, by Robert E. Pitcock, MSFC Memo NR: R-AERO-A-108-63, Huntsville, Ala, 7 Oct 1963 (U)
14. Cornell Aeronautical Laboratory, Transonic Wind Tunnel Tests of a .0175 Scale Pressure Model of the Saturn C-1, Block II Launch Vehicle, by D. L. Millikan, Cornell Report No. HM-1510-V-8, Buffalo, N.Y., 1 Jul 1963
15. NASA Marshall Space Flight Center, Design Criteria – Saturn V, LOR Vehicle: Variation of Normal Force Coefficient and Center of Pressure with Angle of Attack for Mach Numbers 0.5 to 1.93, by R. E. Pitcock, MFSC Memo NR: R-AERO-AD-64-14, Huntsville, Ala, 20 Jan 1964 (U)

16. -----, Experimental Static Longitudinal Stability and Drag Characteristics of the Saturn V/RIFT Vehicle (MSFC Drawing 0347), by J. D. Johnson, MSFC Memo NR: M-AERO-E-241-63, Huntsville, Ala, 12 Sep 1963 (U)
17. -----, Experimental Static Longitudinal Stability and Axial Force Characteristics of the Saturn V, Chemical, RIFT, and Nuclear Vehicles, Anon., MSFC Memo NR: M-AERO-E-244-63, Huntsville, Ala, 12 Sep 1963 (U)
18. -----, Static Longitudinal Stability and Drag Characteristics of the Saturn C-5 Three Stage to Escape Vehicles, Chemical and Nuclear, Anon., MSFC Memo NR: M-AERO-E-83-62, Huntsville, Ala, 10 Jul 1962 (U)
19. -----, Experimental Static Longitudinal Stability and Drag Characteristics on Body Build-up of the Saturn V LOR, Chemical, Three Stage-to-Escape Vehicle, Anon., MSFC Memo NR: M-AERO-E-123-63, Huntsville, Ala, 27 Mar 1963 (U)
20. -----, Presentation of Basic Data from Transonic Wind Tunnel Investigation of Static Longitudinal Stability and Axial Force Characteristics of the Saturn V, Chemical, RIFT, and Nuclear Vehicles, by Josh D. Johnson and James R. Morgan, MSFC Memo NR: M-AERO-E-86-63, Huntsville, Ala, 26 Feb 1963 (U)
21. -----, Presentation of Basic Data from Supersonic Wind Tunnel Investigation of Static Longitudinal Stability and Axial Force Characteristics of the Saturn V Chemical, RIFT, and Nuclear Vehicles (MSFC Project P34), by Josh D. Johnson and James R. Morgan, MSFC Memo NR: M-AERO-E-158-63, Huntsville, Ala, 16 May 1963 (U)
22. -----, Experimental Static Longitudinal Stability and Drag Characteristics of the Saturn V Launch Logistics Vehicle (MSFC Drawing 0297), by Josh D. Johnson, MSFC Memo NR: M-AERO-E-233-63, Huntsville, Ala, 20 Aug 1963 (U)
23. -----, Design Criteria: Contributions of Apollo CM and LES to Saturn Launch Vehicle Aerodynamic Stability and Loads, by Ann C. Seiber and Victor K. Hanson, MSFC Memo NR: R-AERO-AD-64-82, Huntsville, Ala, 18 Aug 1964 (U)
24. Lockheed Missiles & Space Company, Linear Aerodynamic Characteristics for the 2nd and 3rd Design Iteration RIFT Test and Operational Vehicle ML 471-105(01) -107(01), -6(01), by G. W. Morris and R. D. Singley LMSC IDC 53-41-432, Sunnyvale, Calif., 19 Feb 1964 (U)

25. -----, RIFT Systems Analysis, Vol. 3 – Aerodynamics, Anon., LMSC NS P-63-96-Vol. 3, Sunnyvale, Calif., Nov 1963 (U)
26. The Boeing Company, C-5 Fin-Shroud Combinations Wind Tunnel Force Test P-29 – Final Data Release, by Dennis E. Nelson, Boeing Document No. D5-11231, 8 Feb 1963 (U)
27. -----, Saturn V Wind Tunnel Pressure Test No. P-41 – Final Data Release, Volume I, by T. R. Asbjornsen and J. W. Jants, Boeing Document No. D5-11230, 11 Dec 1962 (U)
28. NASA Marshall Space Flight Center, Bending Vibrations, First Stage Saturn IB, Vehicle 201, Anon., MSFC Memo NR: R-AERO-DD-17, Huntsville, Ala, 9 Apr 1964 (U)
29. -----, Vibration Analysis of Saturn V LOR, by Homer Park, MSFC Aero-Astrodynamics Internal Note: R-AERO-1-64, Huntsville, Ala, 6 Jan 1964 (U)
30. -----, Preliminary Saturn IB (Operational) Vehicle Performance, Anon., MSFC Memo NR: R-AERO-DAP, Huntsville, Ala, 15 Jan 1965 (C)
31. -----, Saturn V Performance Summary and Trajectory Data Based on Specification Weights, Anon., MSFC Memo NR: M-AERO-D-1-63, Huntsville, Ala, 29 Apr 1963 (C)
32. Lockheed Missiles & Space Company, Preliminary Data Release for the Transonic Wind Tunnel Tests of the Saturn-Apollo 5% Model, by J. P. Reding, LMSC/802367 (TM 53-40-122), Sunnyvale, Calif., Nov 1962 (U)
33. -----, Preliminary Data Release for the Supersonic Wind Tunnel Tests of the Saturn-Apollo 5% Model, by J. P. Reding, LMSC/802393 (TM 53-40-123), Sunnyvale, Calif., Dec 1962 (U)
34. NASA Marshall Space Flight Center, Bending Vibrations, SA-8 and SA-9 Vehicles, by George F. McDonough, MSFC Memo NR: R-AERO-DD-2, Huntsville, Ala, 3 Mar 1964 (U)

35. -----, Two-Stage Saturn I Orbital Trajectory (SA-6), Anon., MSFC Memo NR: M-AERO-TT-863, Huntsville, Ala, Mar 1963 (C)
36. Lockheed Missiles & Space Company, Static Loads on the Saturn I - Apollo Launch Vehicle, by J. P. Reding and Lars-Eric Ericsson, LMSC/803185 (TM 53-40-143), Sunnyvale, Calif., Aug 1963 (U)

Appendix A  
NOTATION

C	force coefficient = Force/ $\rho_\infty (U_\infty^2/2) S$
D <sub>REF</sub>	reference length (6.5278 m for Saturn-IB and 10.0584 m for Saturn-V)
D <sub>a</sub>	equivalent damping derivative = $(\zeta_a/\zeta_c)/(-\rho U_\infty S/4\omega \tilde{m})$
L	longitudinal distance (m)
M	Mach number
$\tilde{m}$	generalized mass (kg - sec <sup>2</sup> /m)
P	pressure (kg/m <sup>2</sup> )
q	dynamic pressure (kg/m <sup>2</sup> )
$\bar{q}$	average dynamic pressure (kg/m <sup>2</sup> )
S	reference area = $\pi D_{REF}^2/4$ (m <sup>2</sup> )
t	time (sec)
U	velocity (m/sec)
$\bar{U}$	average velocity (m/sec)
x	longitudinal coordinate (m)
Z	vertical displacement (m)
$\alpha$	angle of attack (deg or radian)
$\beta$	equivalent spike deflection angle (deg or radian)
$\Delta$	incremental unit, e.g., $\Delta t$ = increment of time
$\rho$	density (kg-sec <sup>2</sup> /m <sup>4</sup> )
$\omega$	free-free bending frequency (radian/sec)
$\zeta_a$	aerodynamic damping
$\zeta_c$	critical damping
$\theta$	rotation angle (deg or radian)

Subscripts

A	axial force
a	attached flow

Subscripts (Cont'd)

ac	aerodynamic center
c	denotes shock location on cylinder
L	leeward
m	pitching moment
N	normal force or nose
0	at $\alpha = 0^\circ$
QS	quasi-steady
s	separated flow
T	total
W	windward
1	denotes conditions on attached flow cylinder
2	denotes condition at shock location
$\infty$	undisturbed flow

Superscripts

i induced, e.g.,  $\Delta^i C_N$  = separation induced normal force

Appendix B  
ANALYSIS OF THE SATURN-I (SA-8 AND SA-9) CONFIGURATION

At the request of the NASA Marshall Space Flight Center, an additional Saturn - Apollo configuration (for Flights SA-8 and SA-9) was analyzed along with the Saturn-IB and Saturn-V configurations. This configuration is shown in Fig. B-1. The mode shapes were obtained from Ref. 34, and the previous Saturn-I trajectory (Ref. 35) was assumed. The configuration change relative to the "current flight configuration" of Ref. 1 amounted to a shortening of the service module by 0.077 calibers. The major effect of the configuration change was to alter the load on the interstage frustum between the service module and the S-IV stage. The data from Refs. 5 and 6 were used to adjust for cylinder length. The new frustum load is compared to that of the previous Saturn-I configuration in Fig. B-2. The switch in the trend of the data between subsonic and supersonic Mach numbers is the result of critical cylinder length effects (Ref. 36). Figure B-3 indicates that the Saturn-I (SA-8 and SA-9) configuration is aerodynamically damped at  $\alpha = 0^\circ$  over the critical Mach number range ( $0.8 \leq M \leq 2.0$ ).

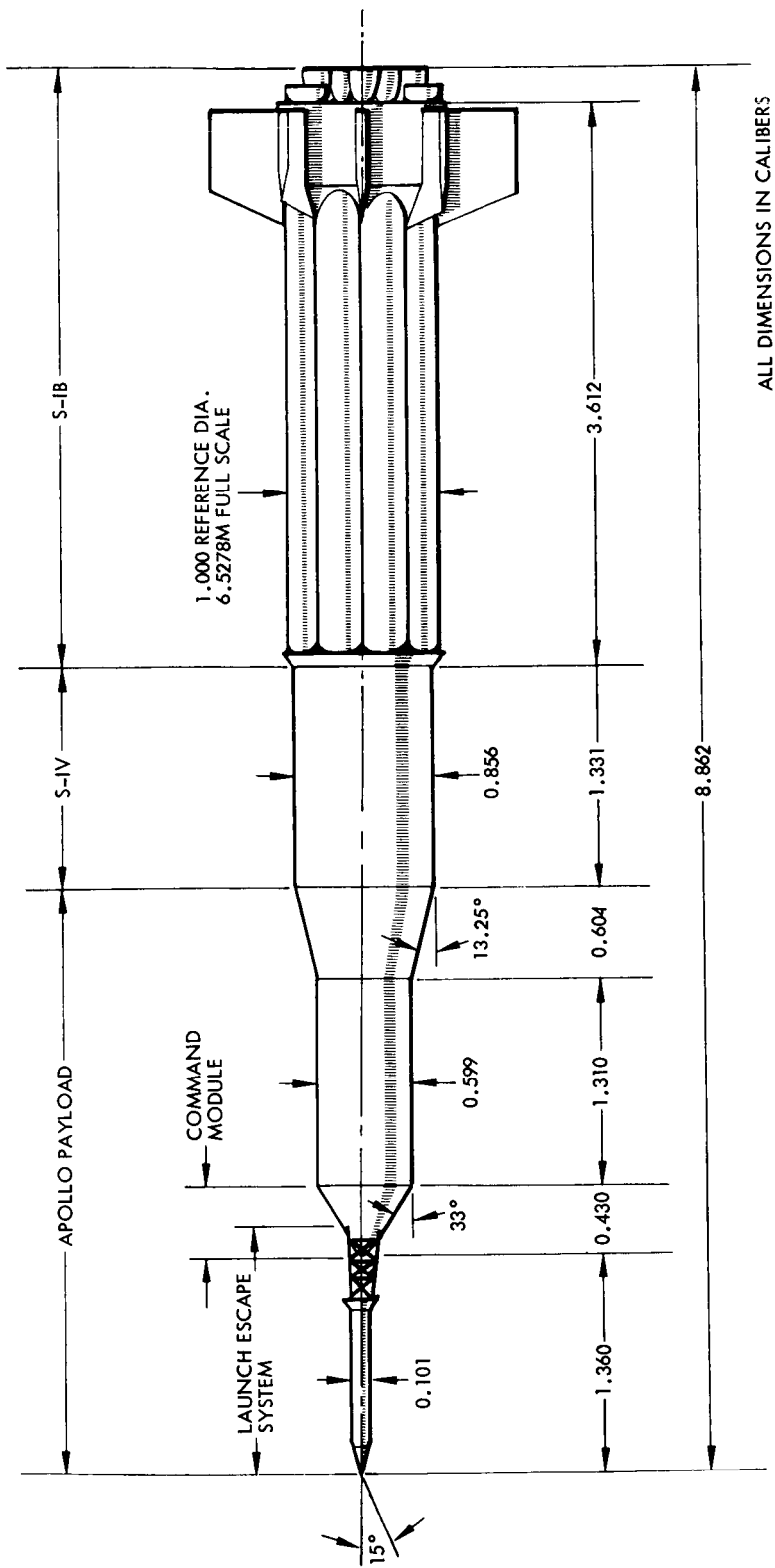


Fig. B-1 Saturn-I (SA-8 and SA-9) Configuration

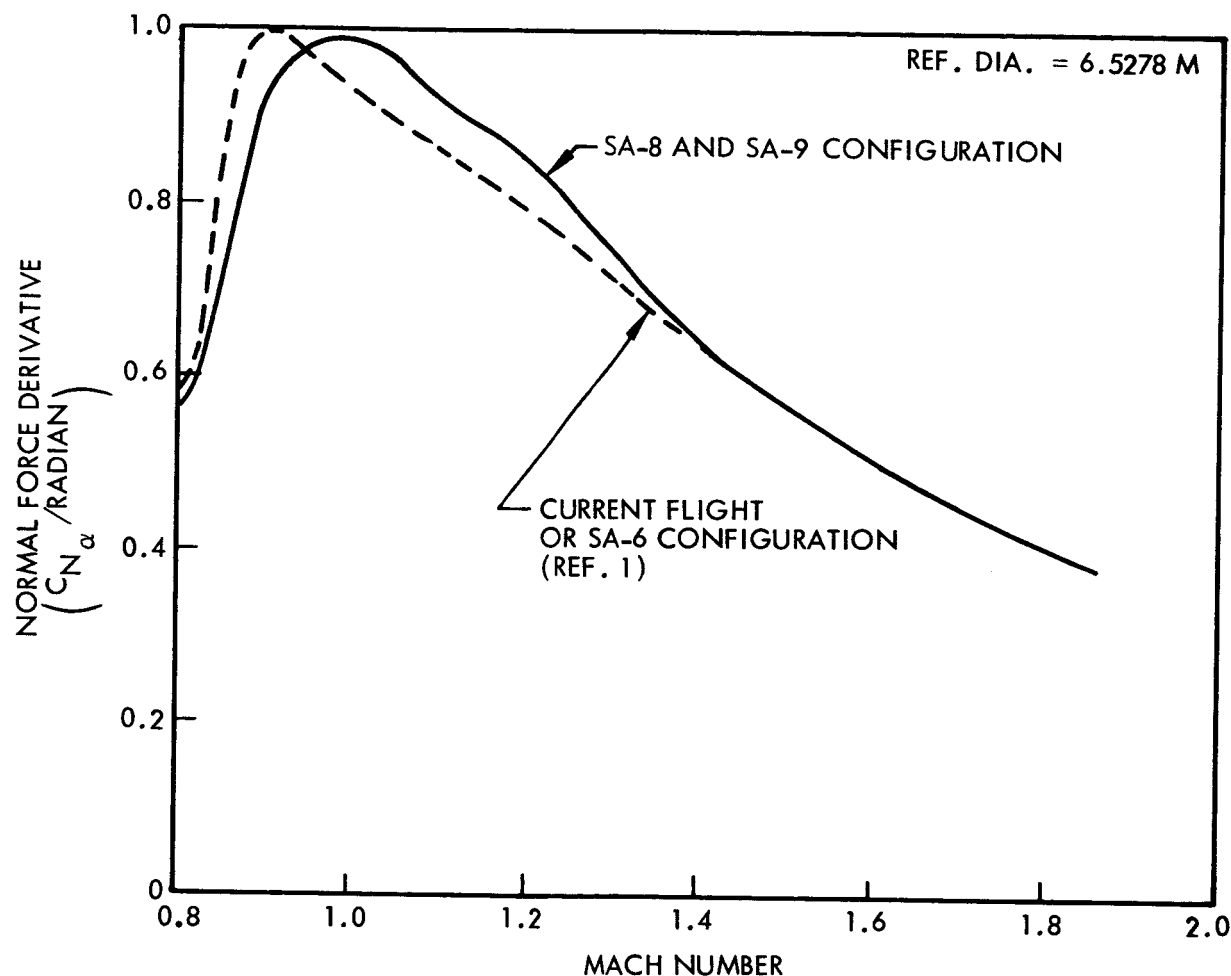


Fig. B-2 Saturn-I Service Module – S-IV Interstage Frustum Loads

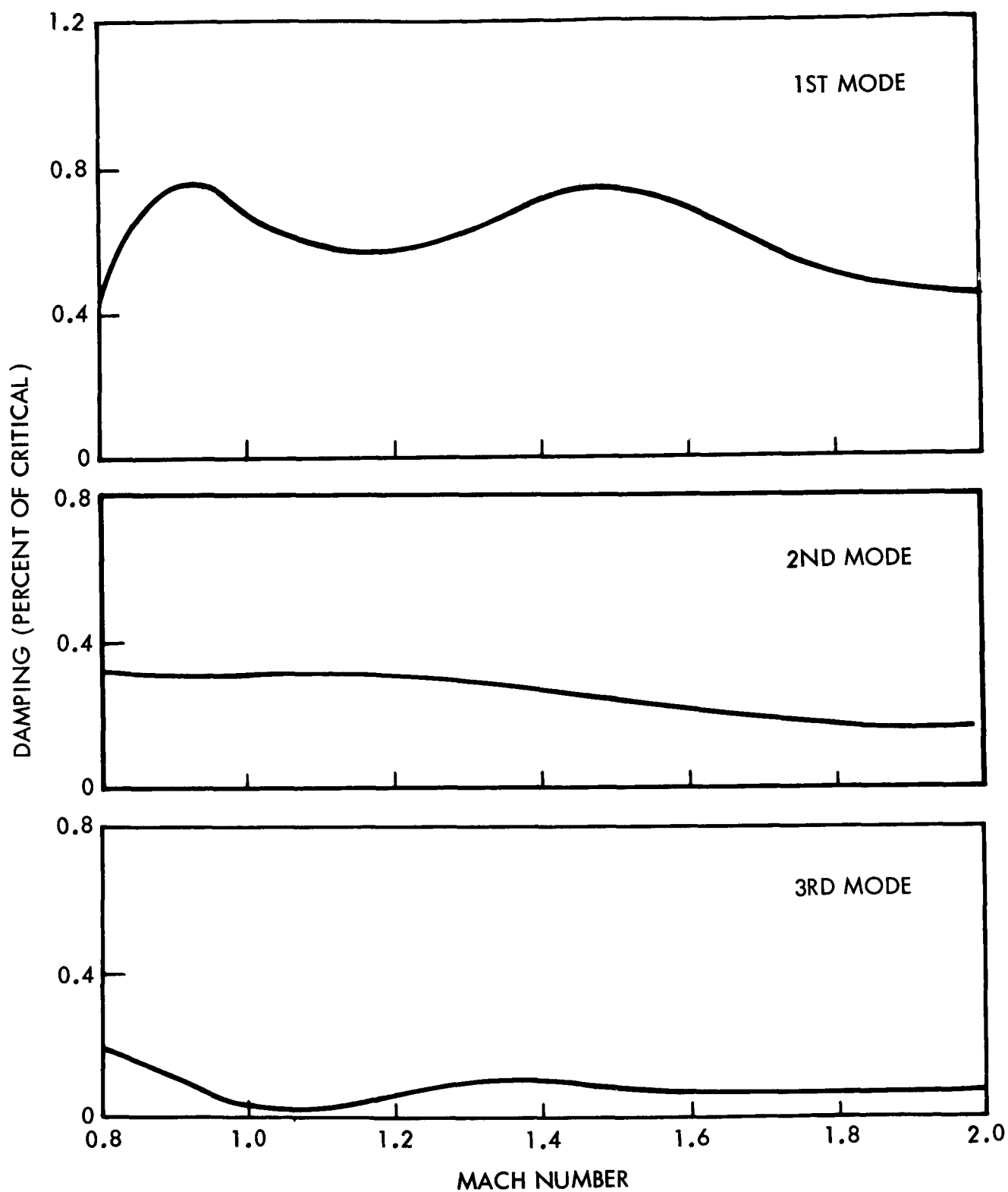


Fig. B-3 Saturn I - Apollo (SA-8 and SA-9) Damping  
at  $\alpha = 0^\circ$

Appendix C  
DOCUMENTATION OF SATURN-IB LUMPED LOADS

The  $\alpha = 0^\circ$ , lumped load representation used in computing the Saturn-IB damping is documented in this Appendix. Figure C-1 relates the lumped loads to the general Saturn-IB force distribution. Both local and induced lumped loads are plotted in Figs. C-2 through C-4, and their centers of pressure appear in Fig. C-5. Figure C-6 presents the local and induced axial force moments on the command module and interstage flares, and Fig. C-7 shows the velocity ratios for each of the separated regions.

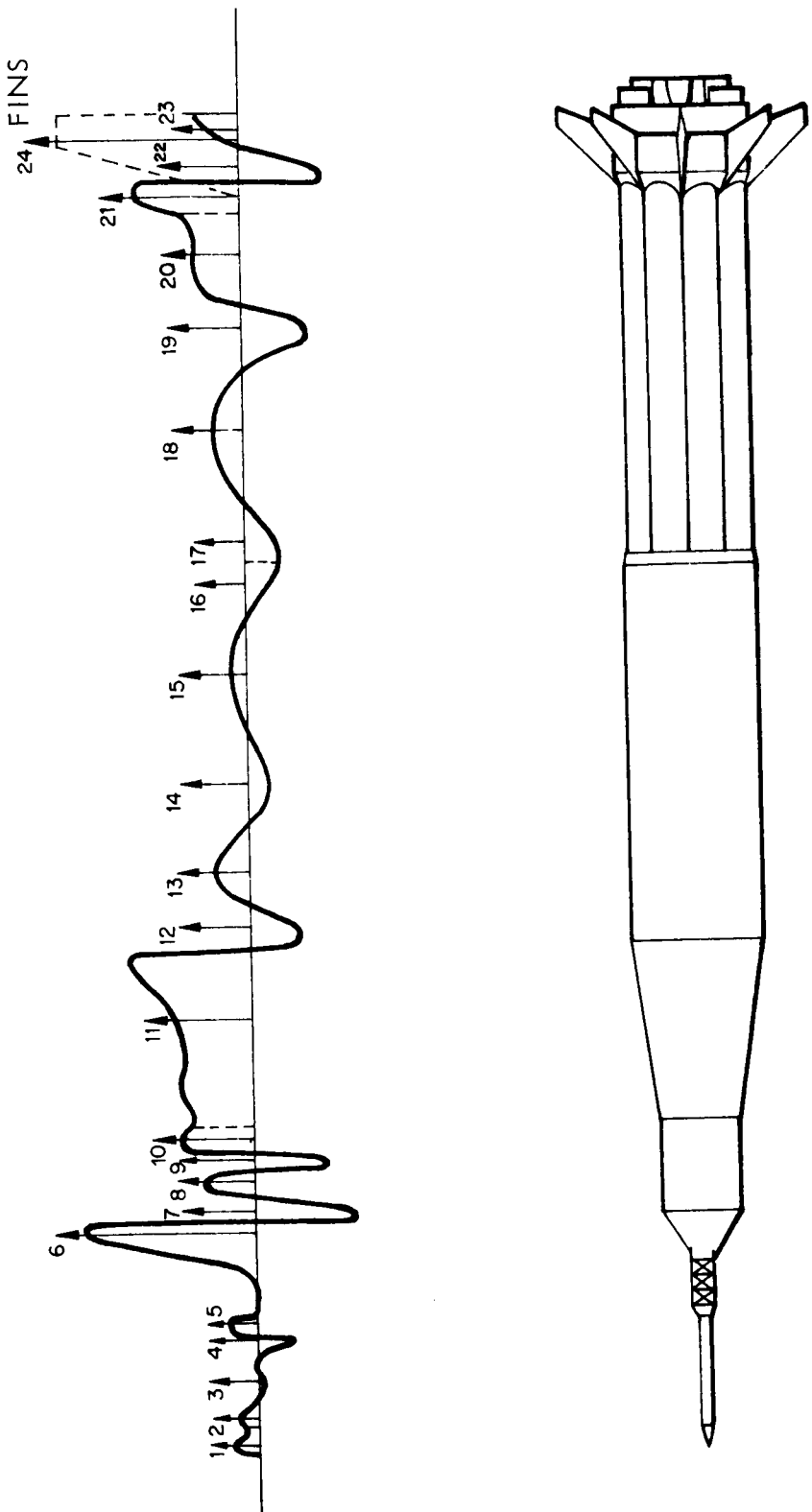


Fig. C-1 Saturn-IB, Definition of Lumped Normal Force Vectors

C-2

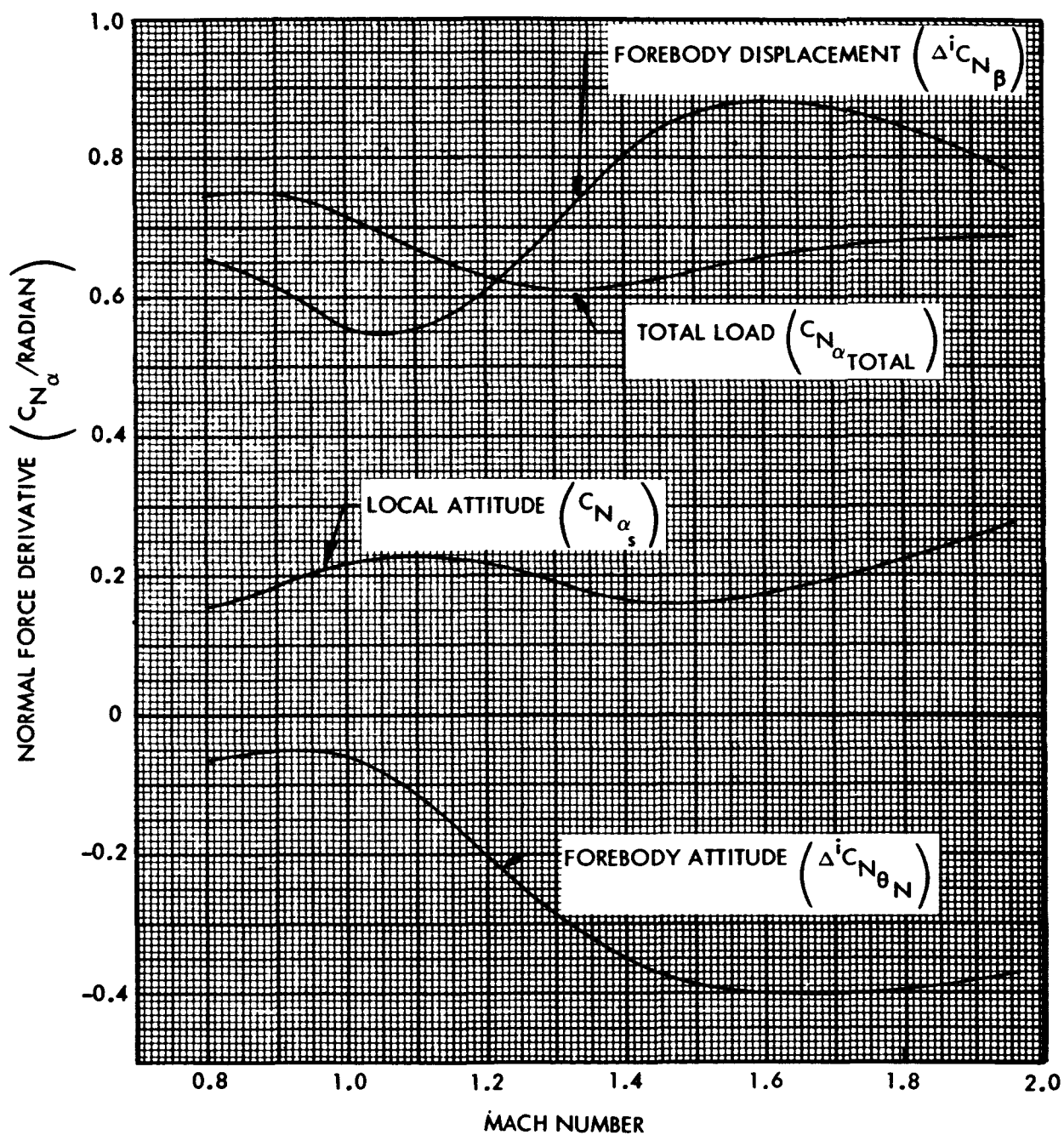


Fig. C-2 Saturn-IB Local and Forebody-Dependent Command Module Loads at  $\alpha = 0^\circ$

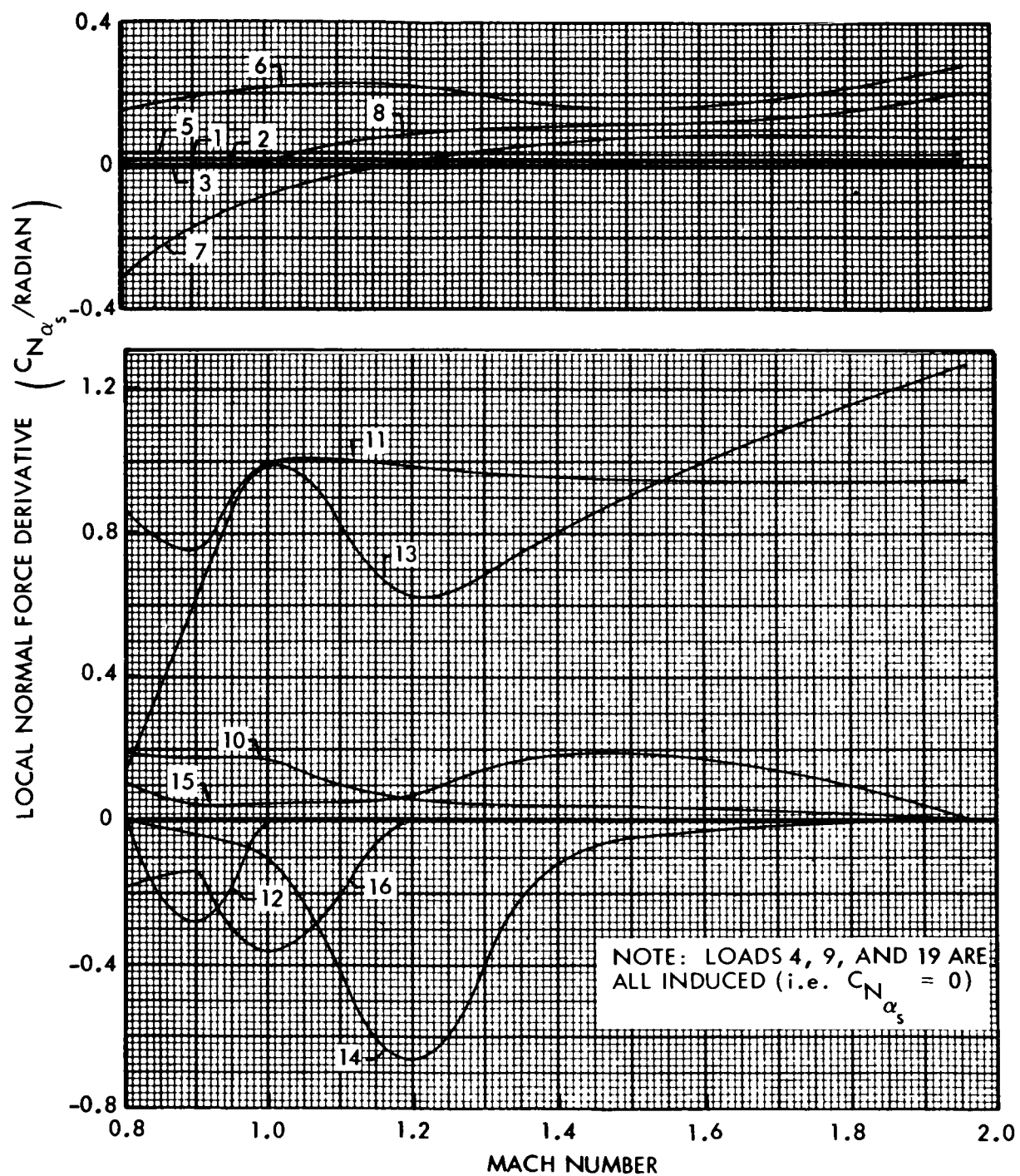


Fig. C-3 Saturn-IB Local Normal Force Derivatives at  $\alpha = 0^\circ$

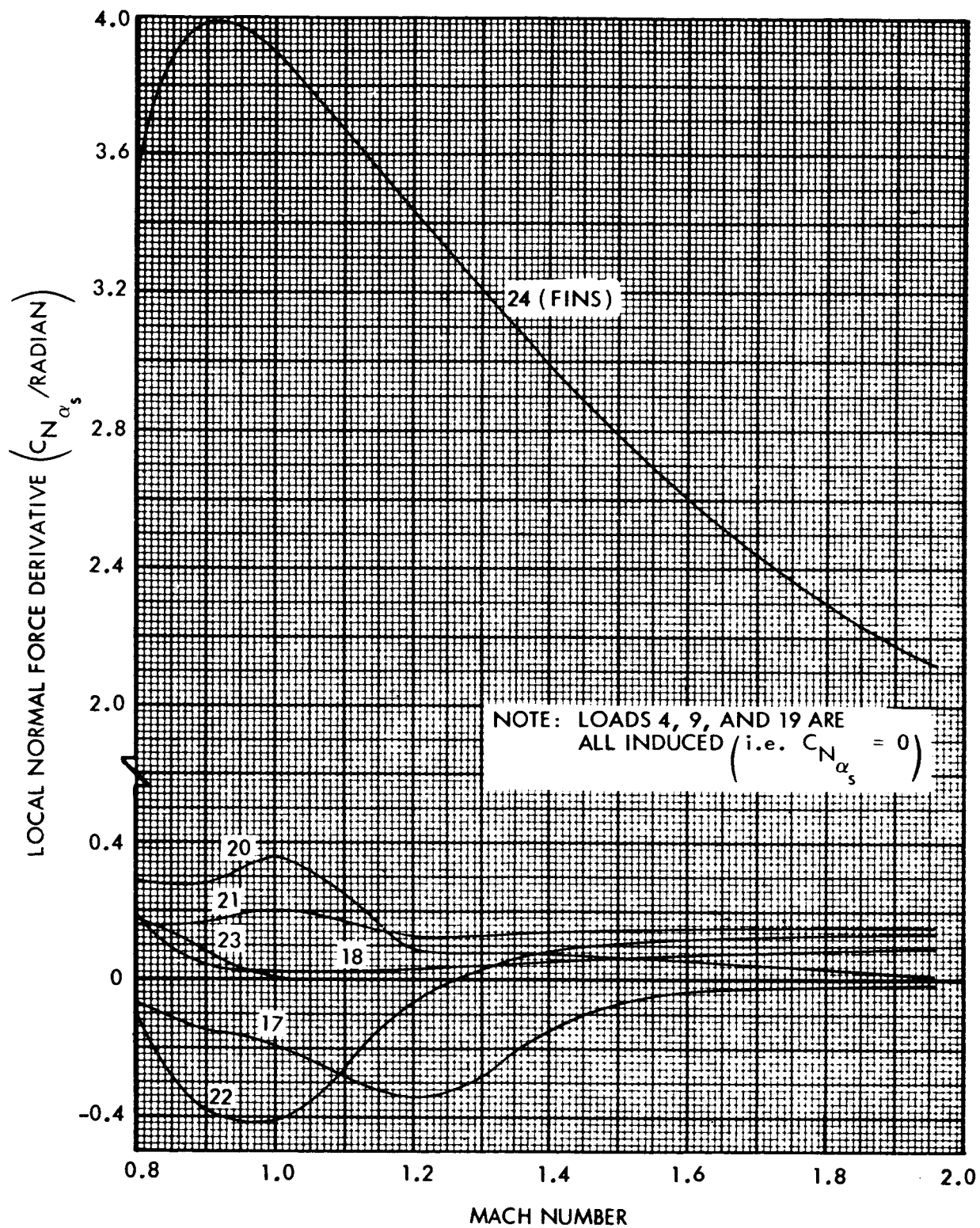


Fig C-3 Saturn-IB Local Normal Force Derivatives at  $\alpha = 0^\circ$  (cont.)

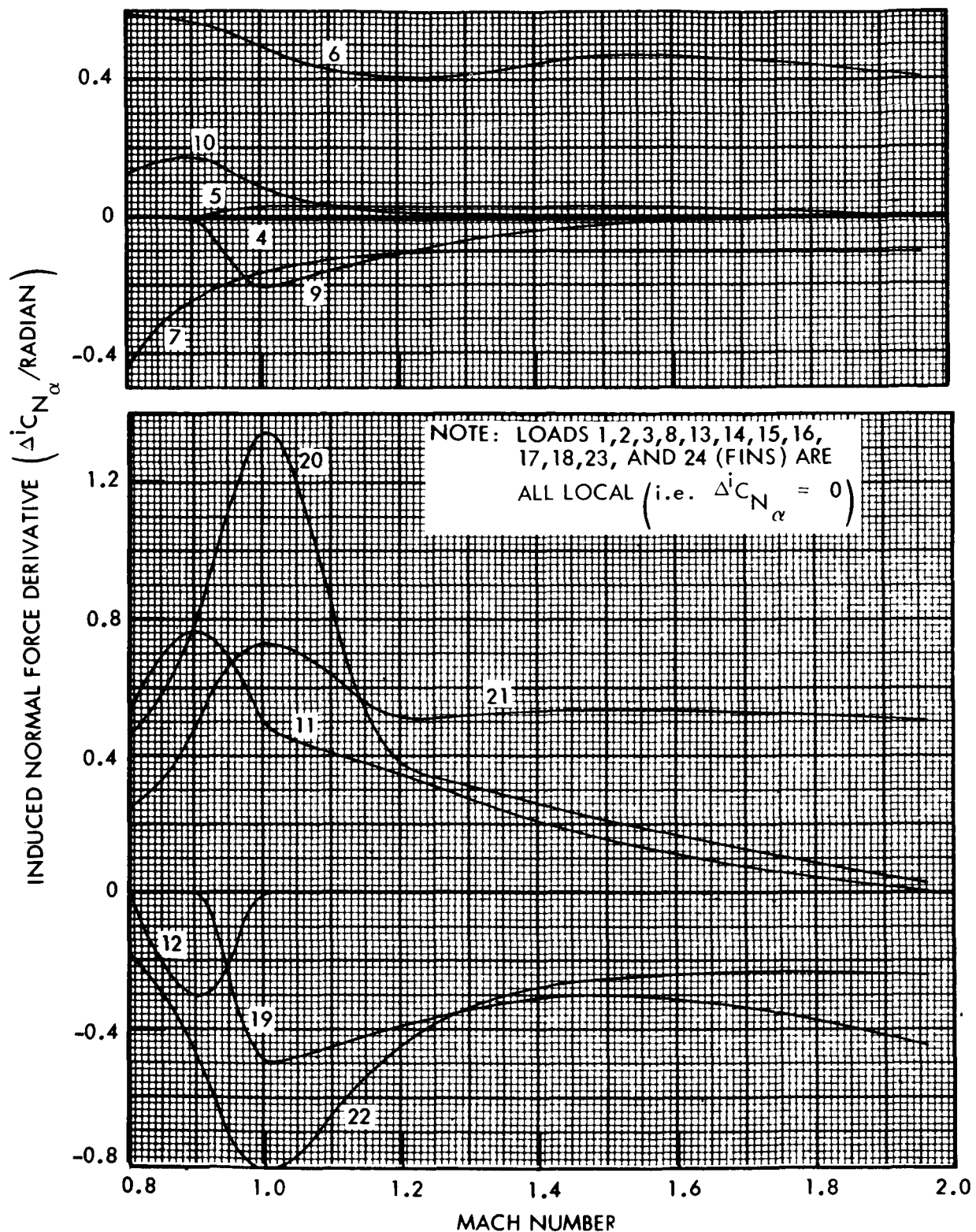
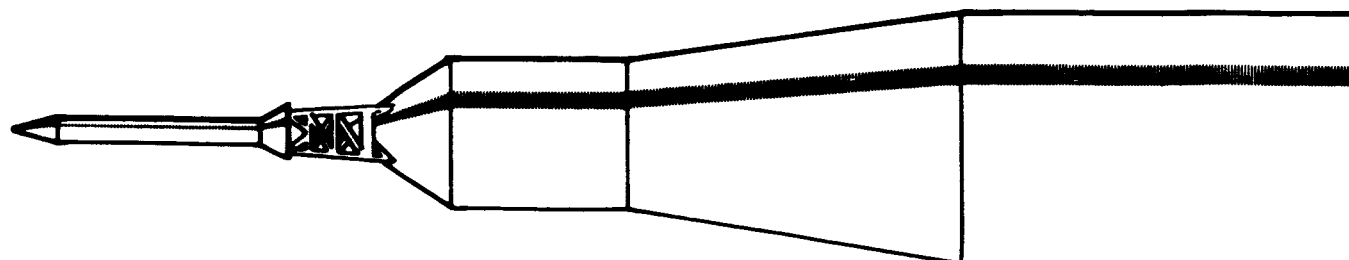
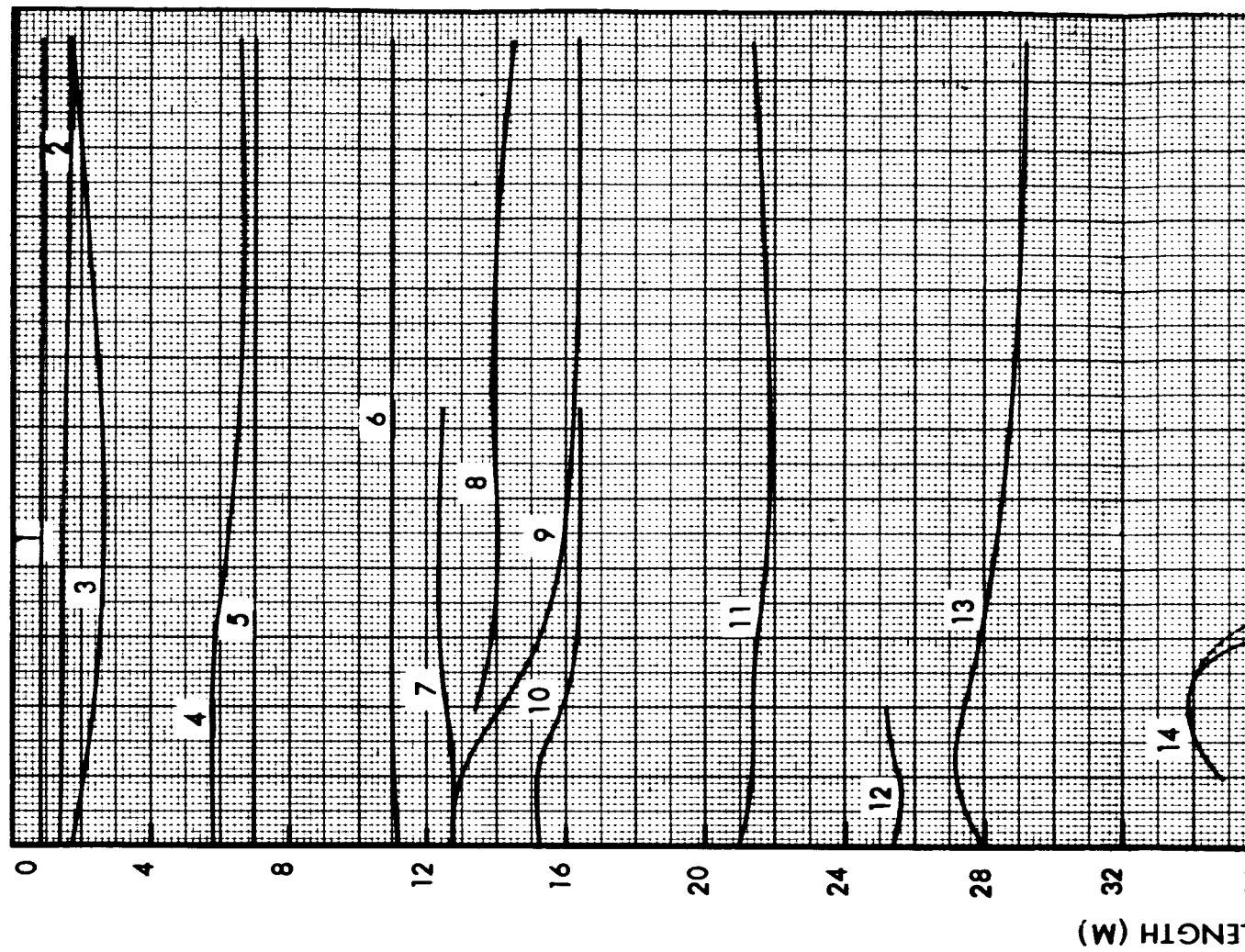


Fig. C-4 Saturn-IB Induced Normal Force Derivatives at  $\alpha = 0^\circ$



C-1  
O

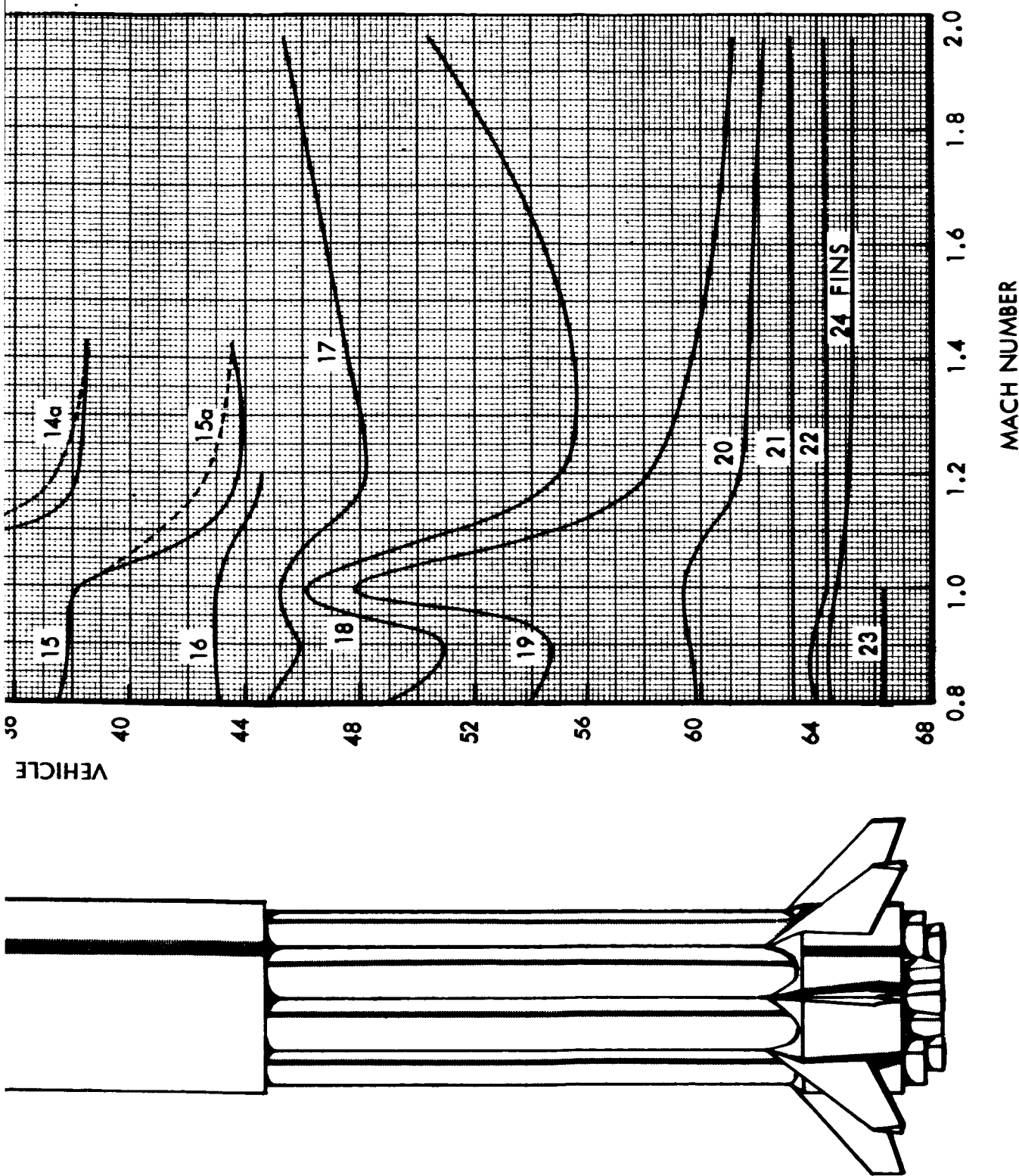


Fig. C-5 Saturn-IB Lumped Load Centers of Pressure at  $\alpha = 0^\circ$

C-7

C-8 ②

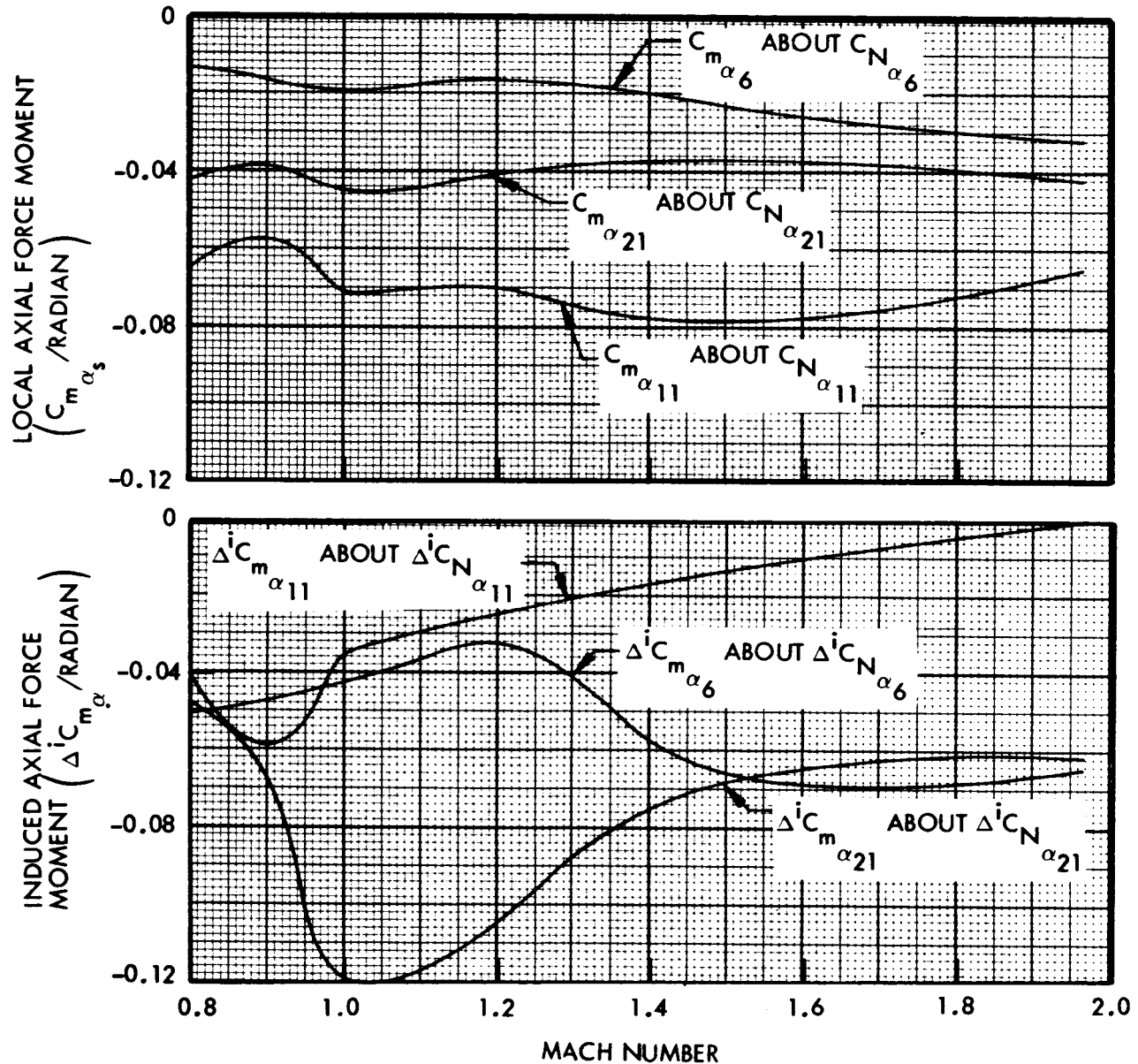


Fig. C-6 Saturn-IB Local and Induced Command Module and Flare Axial Force Moment Derivatives at  $\alpha = 0^\circ$

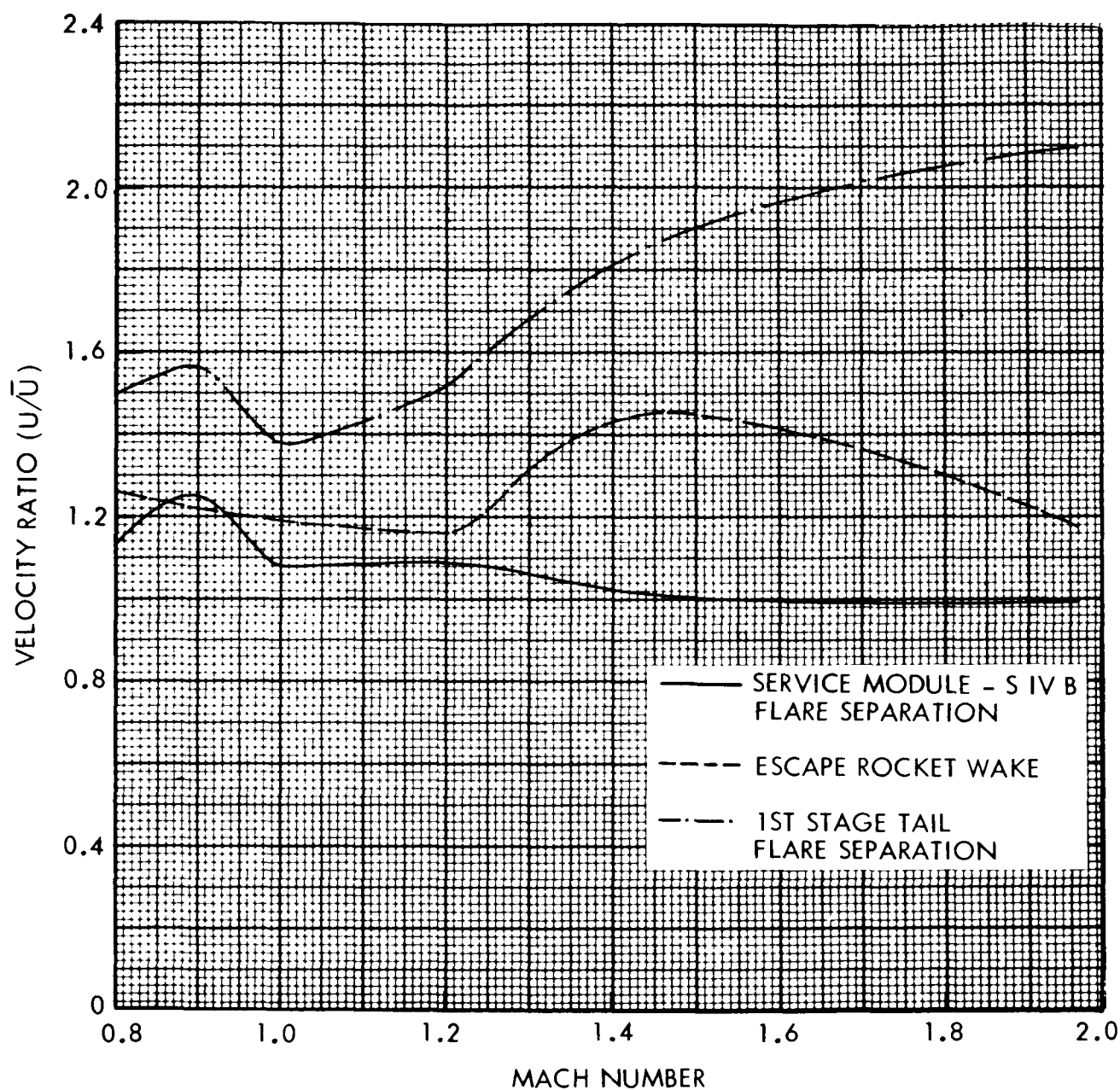


Fig. C-7 Saturn-IB Separated-Flow Velocity  
Ratios at  $\alpha = 0^\circ$

Appendix D  
DOCUMENTATION OF SATURN-V LUMPED LOADS

The  $\alpha = 0^\circ$ , lumped load representation used in computing the Saturn-V damping is documented in this Appendix. Figure D-1 relates the lumped loads to the general Saturn-V force distribution. Both local and induced lumped loads are plotted in Figs. D-2 through D-4, and their centers of pressure appear in Fig. D-6. Figure D-5 presents the local and induced axial force moments on the command module and interstage flares, and Fig. D-7 shows the velocity ratios for each of the separated regions.

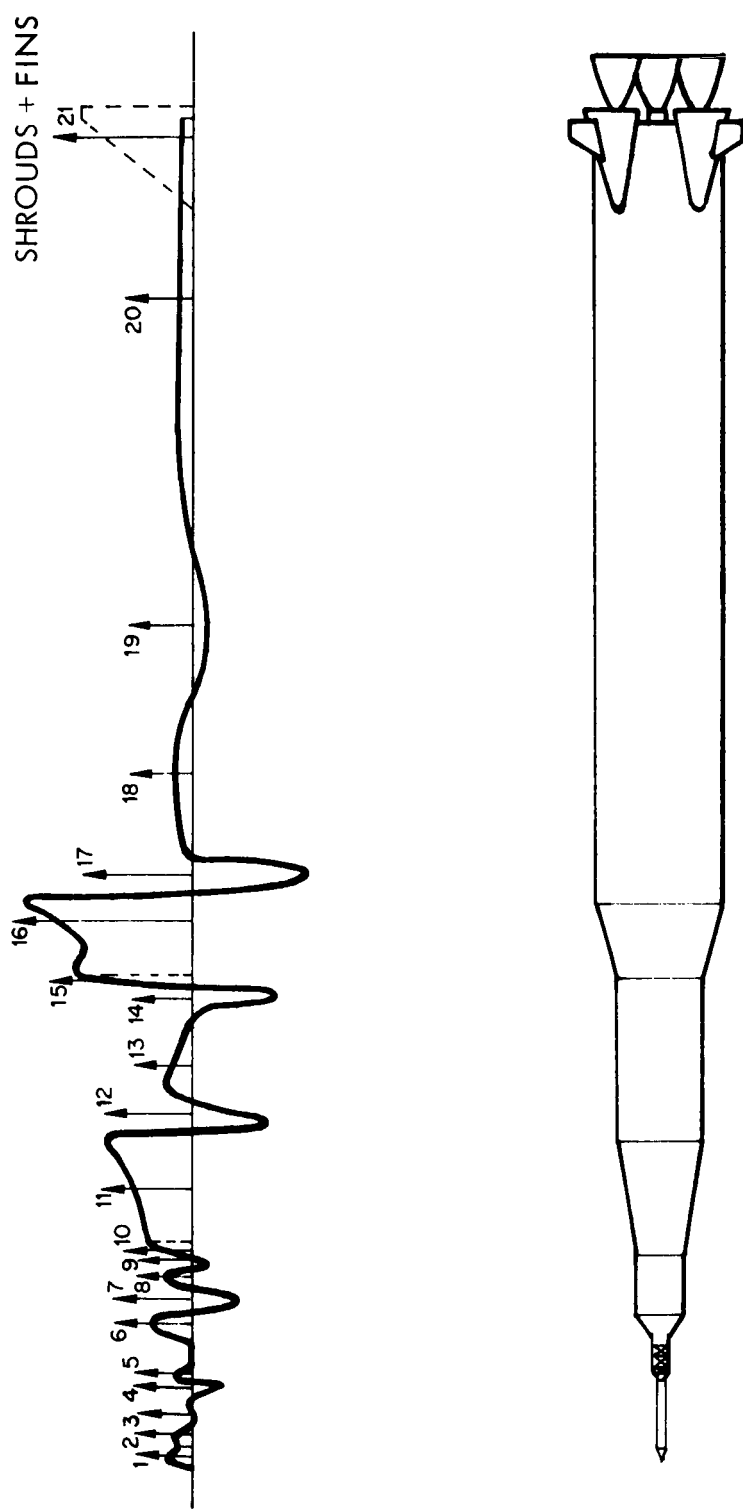


Fig. D-1 Saturn-V, Definition of Lumped Normal Force Vectors

D-2

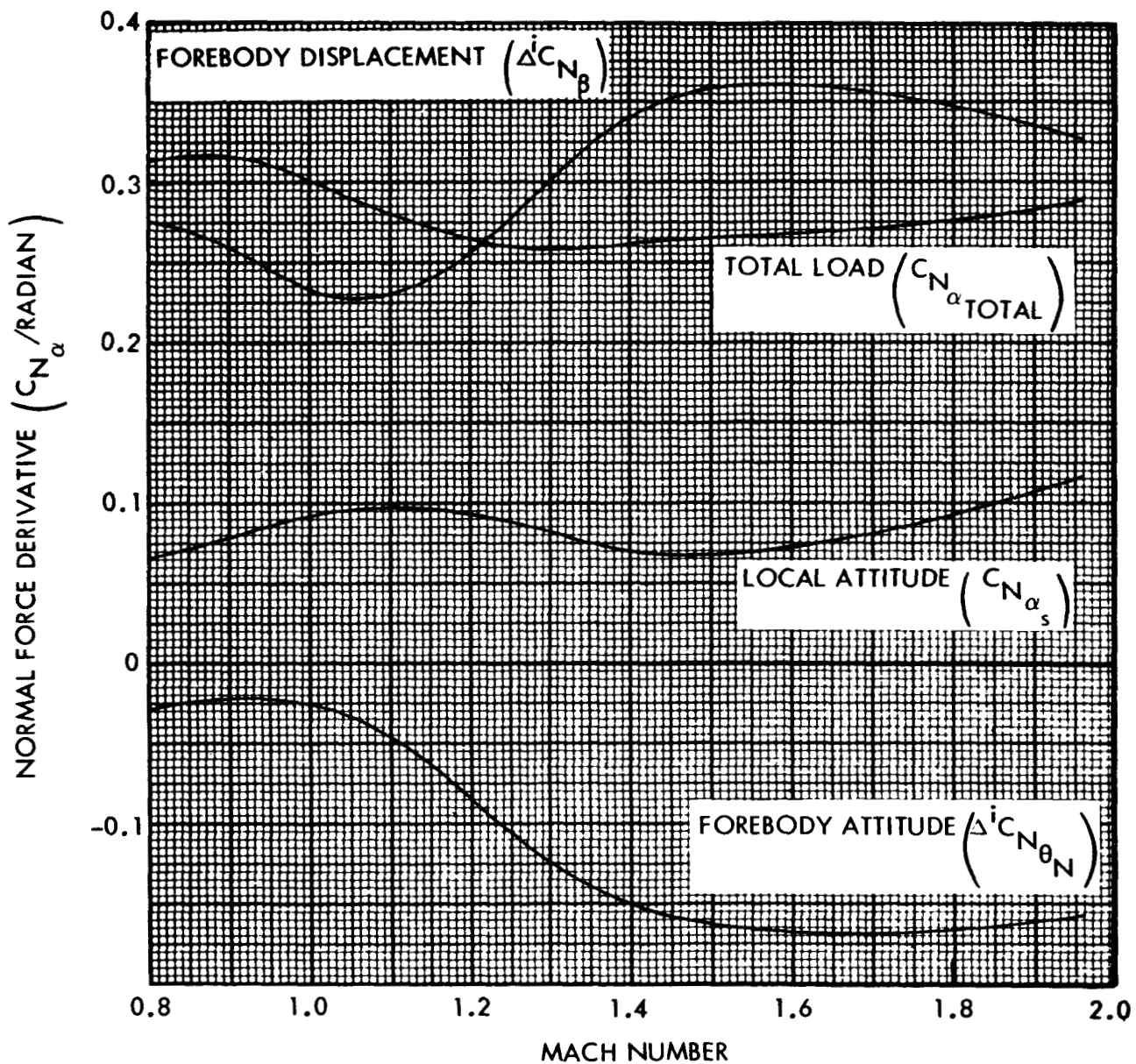


Fig. D-2 Saturn-V Local and Forebody-Dependent Command Module Loadings

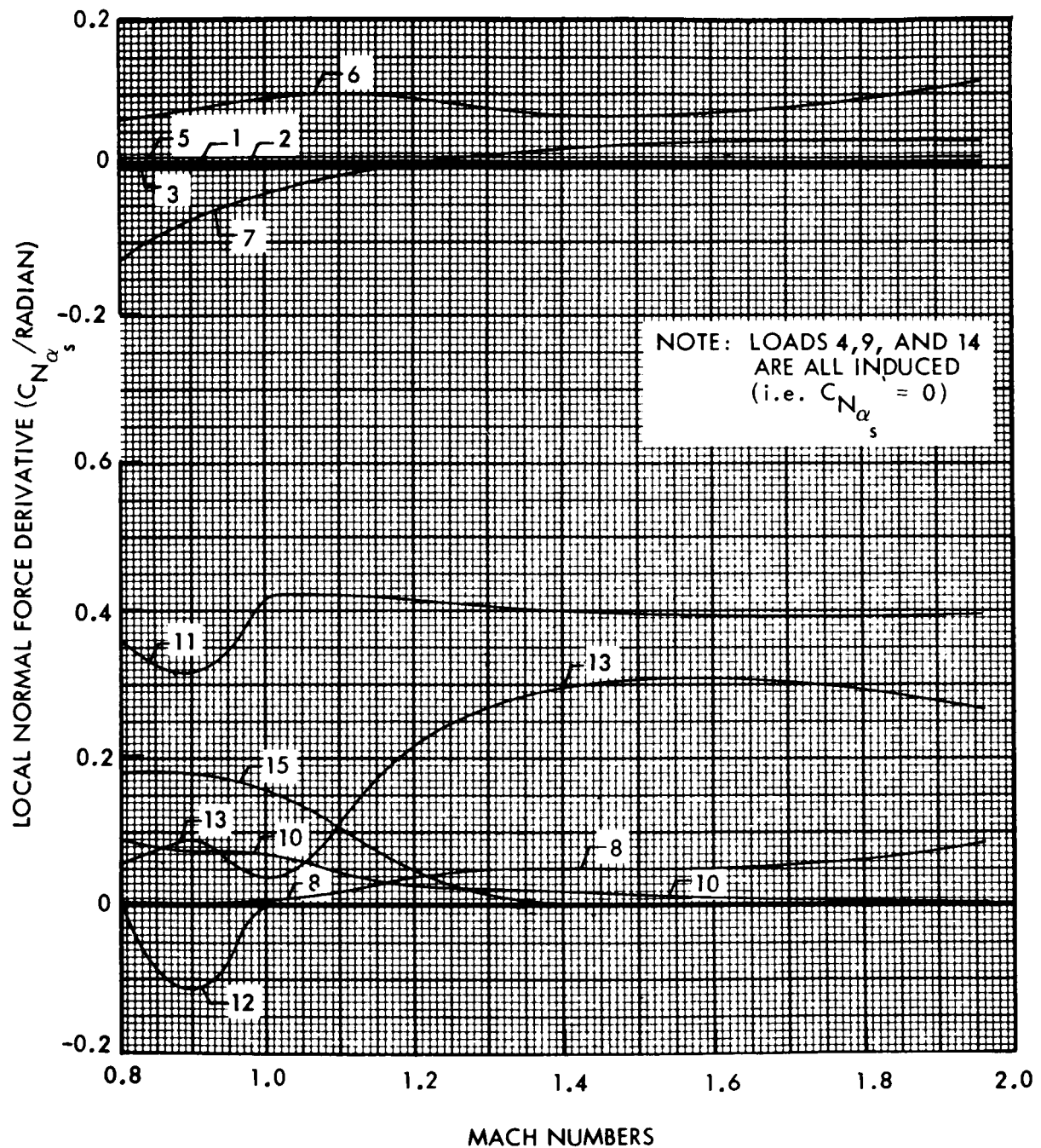
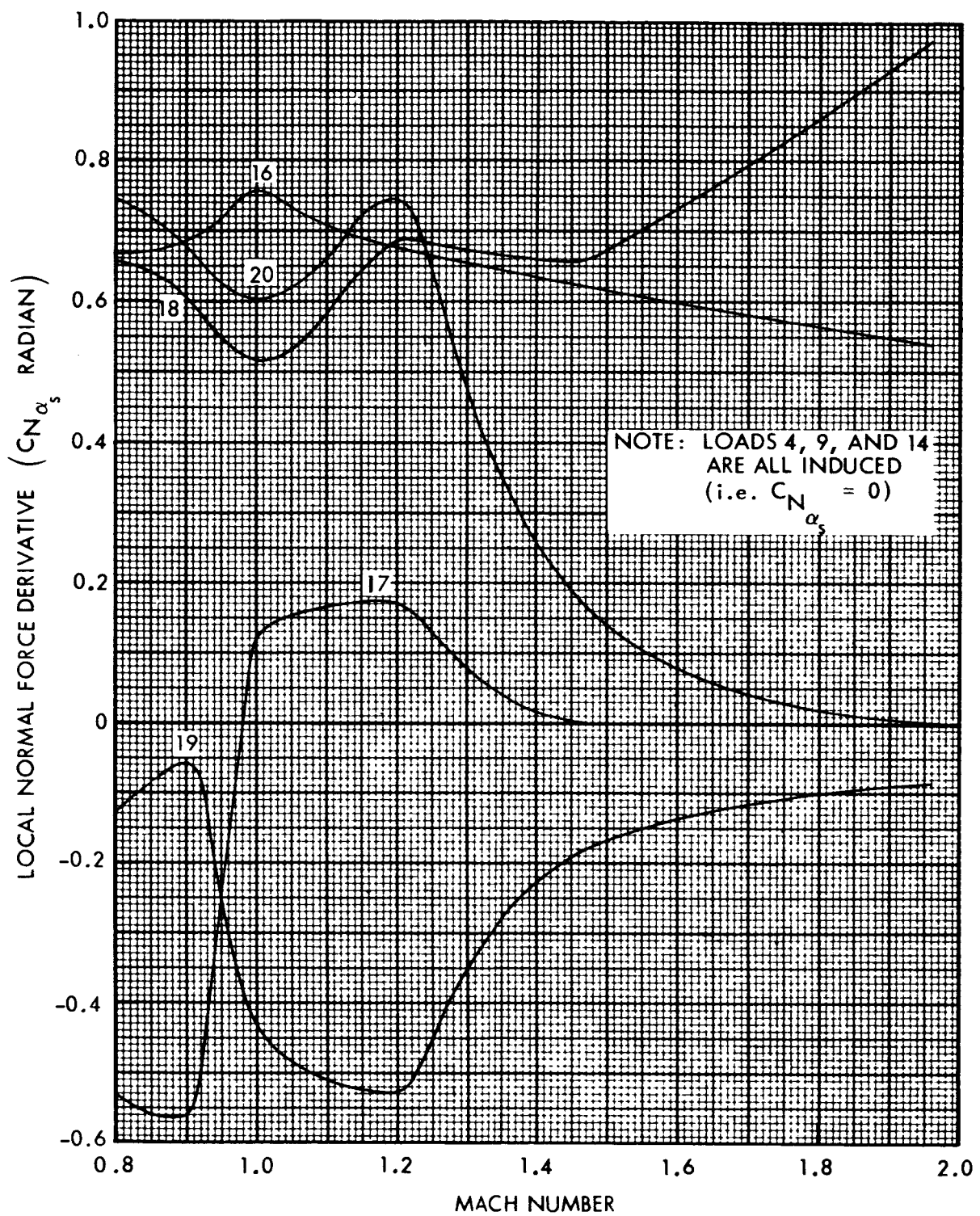
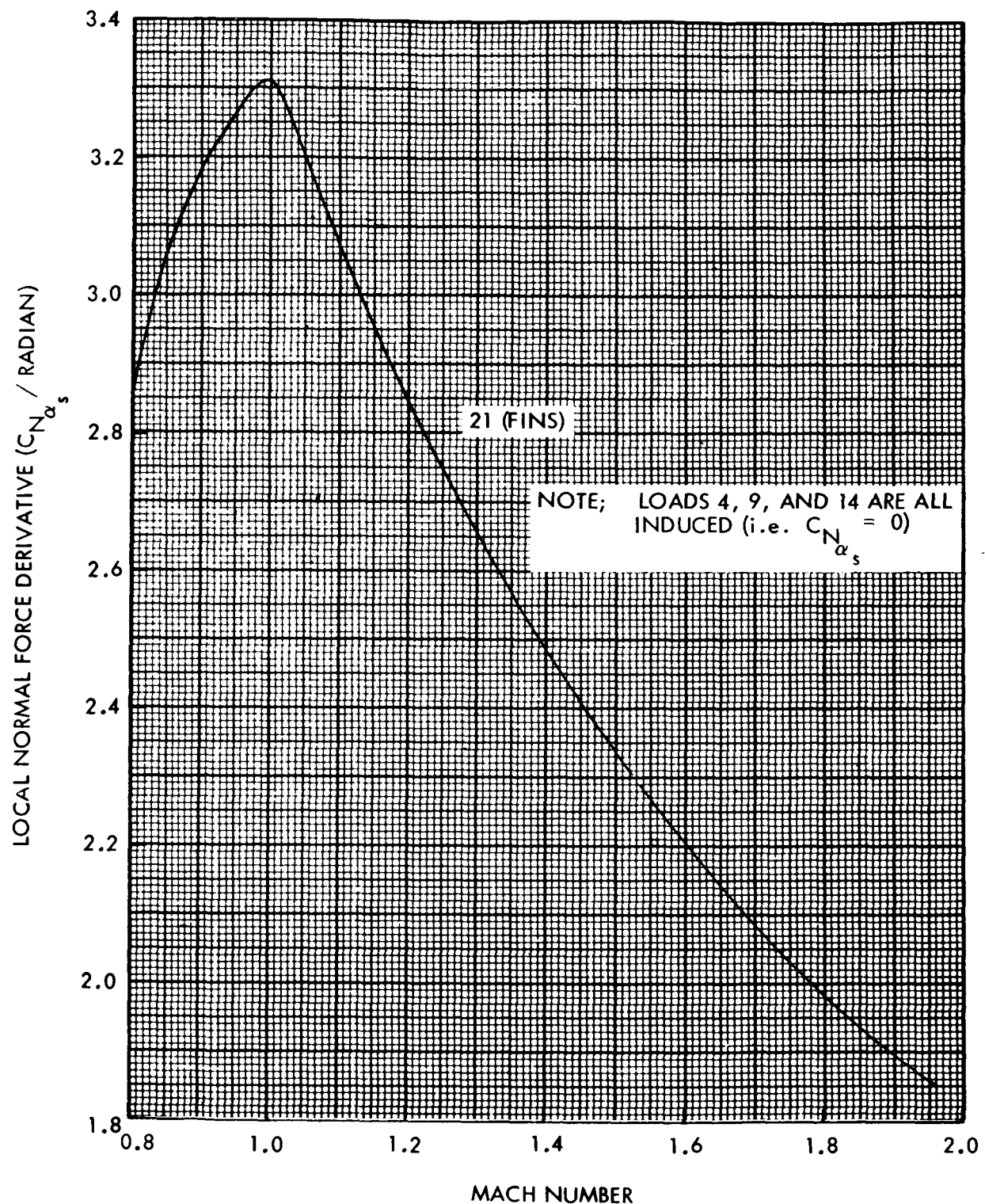
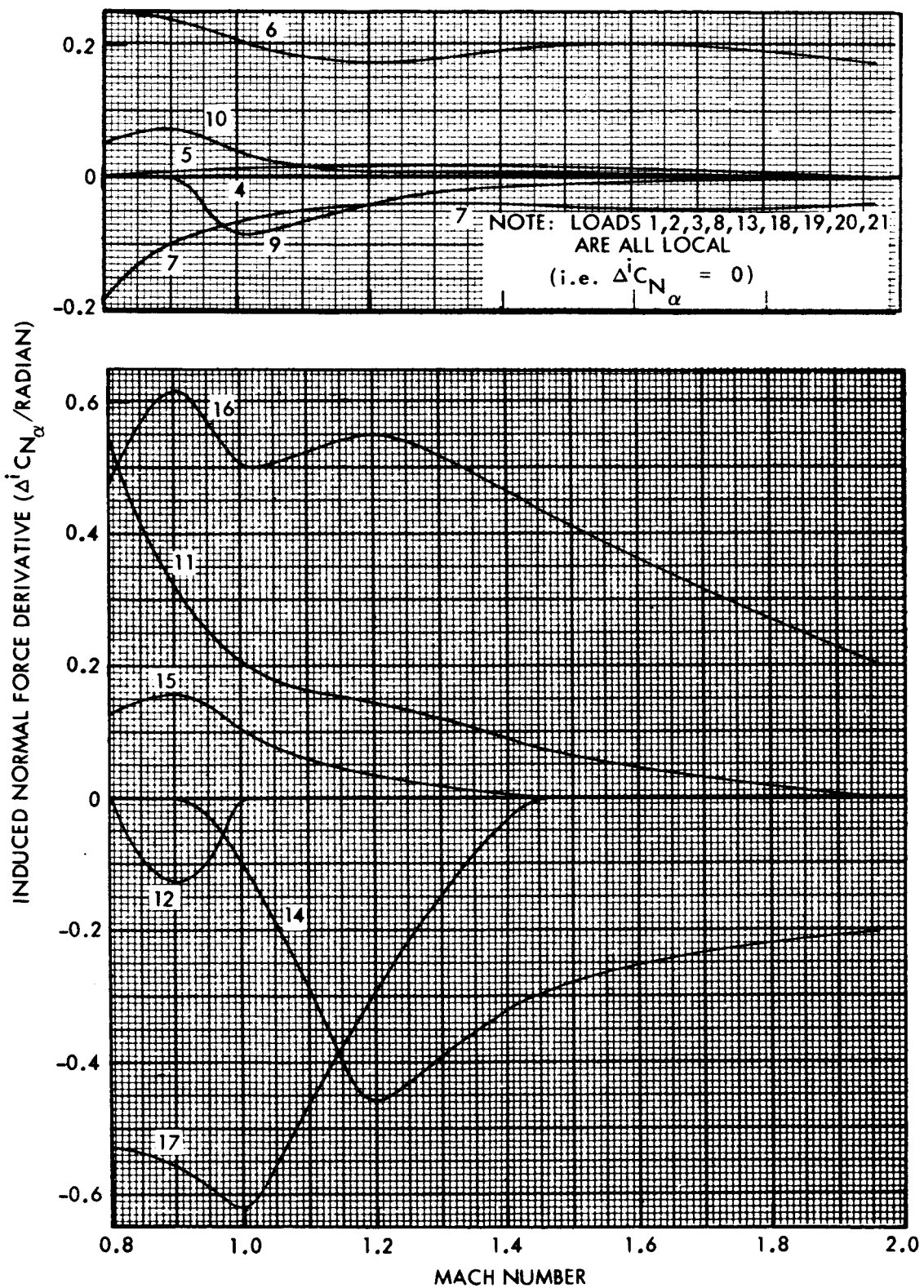


Fig. D-3 Saturn-V Local Normal Force Derivatives at  $\alpha = 0^\circ$

Fig. D-3 Saturn-V Local Normal Force Derivatives at  $\alpha = 0^\circ$  (Cont.)

Fig. D-3 Saturn-V Local Normal Force Derivatives at  $\alpha = 0^\circ$  (Cont.)

Fig. D-4 Saturn-V Induced Normal Force Derivatives at  $\alpha = 0^\circ$

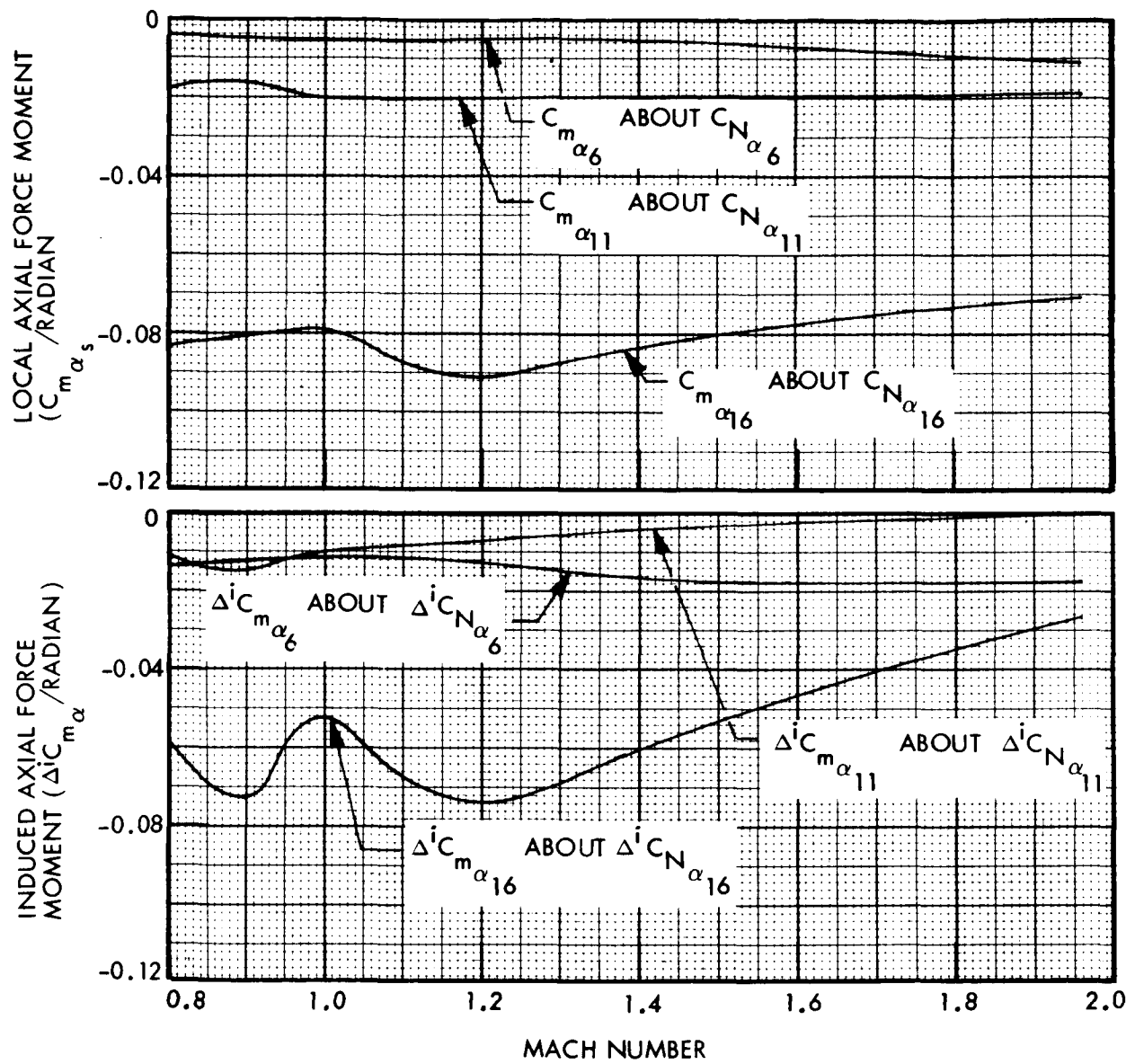
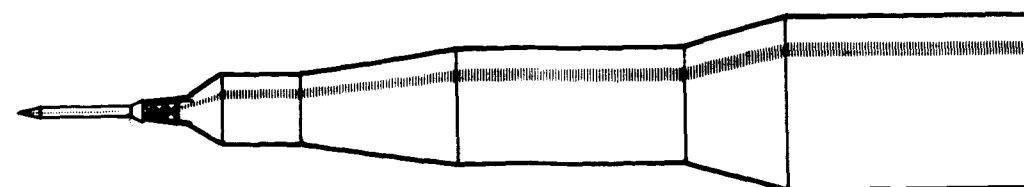
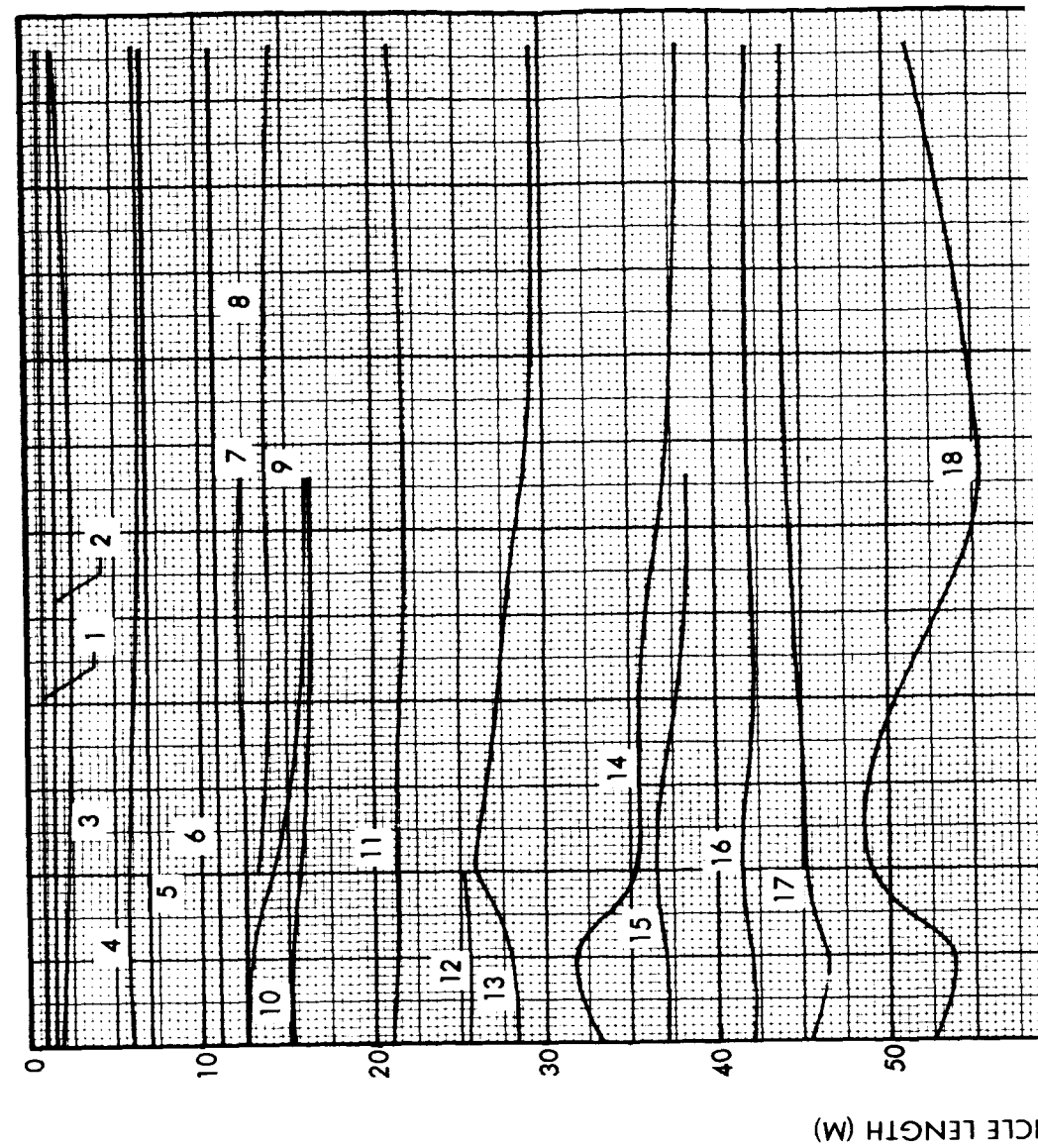


Fig. D-5 Saturn-V Local and Induced Command-Module and Flare Axial Force Moment Derivatives at  $\alpha = 0^\circ$



D-9①

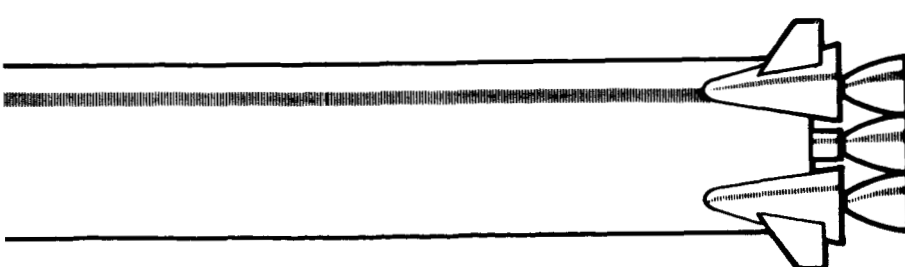
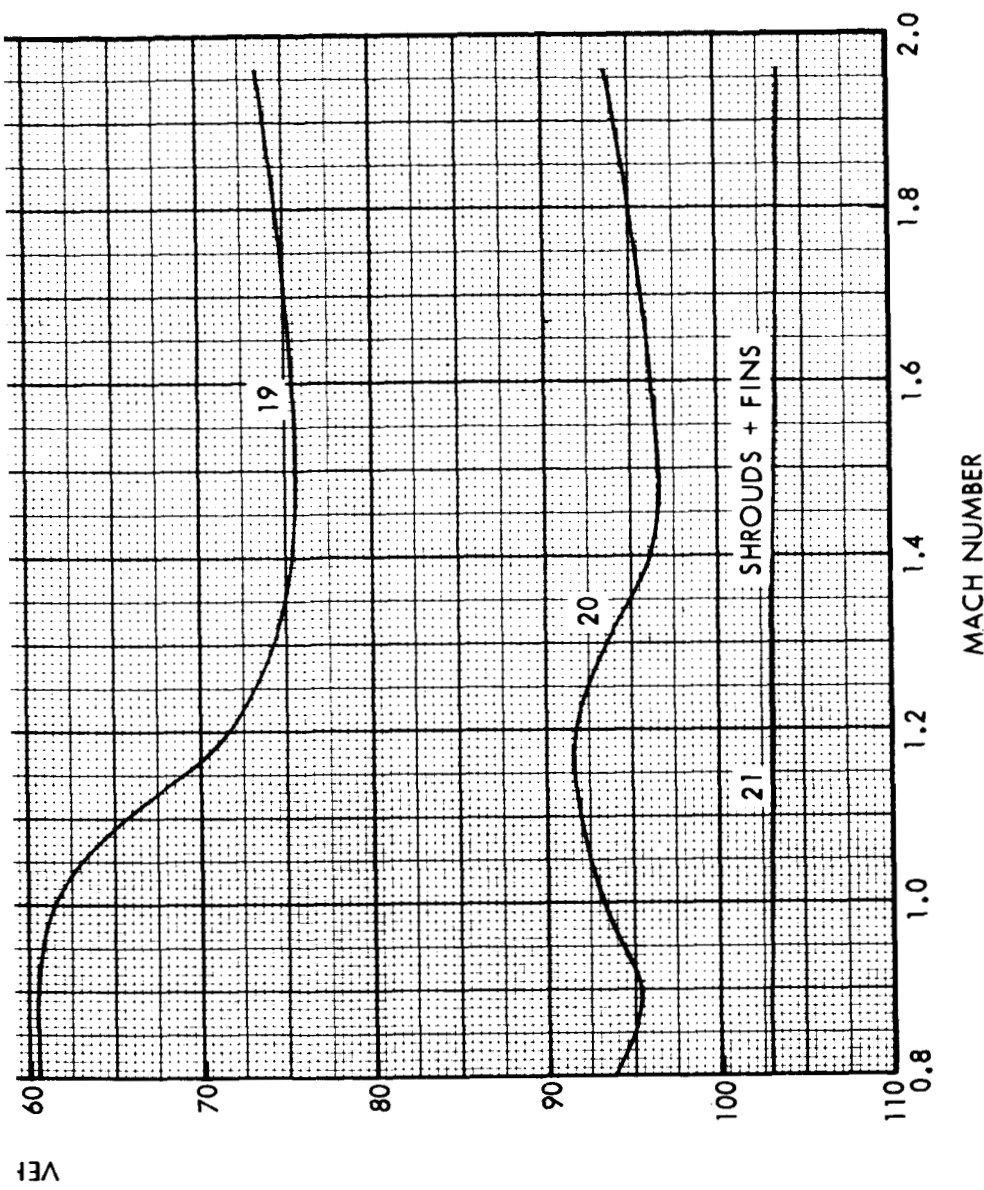
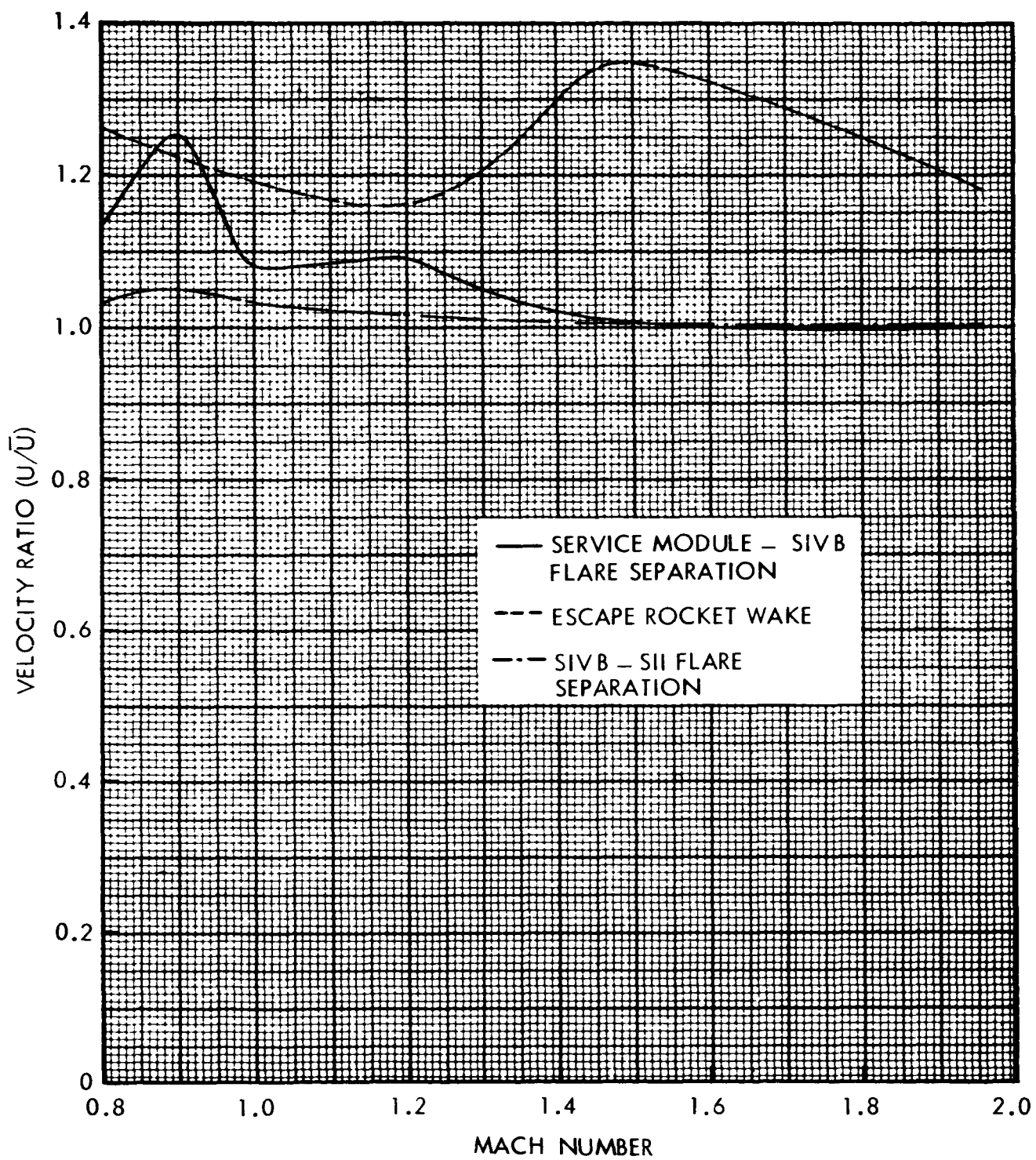


Fig. D-6 Saturn-V Lumped Load Centers of Pressure  $\alpha = 0^\circ$

D-9

D-10  
②

Fig. D-7 Saturn-V Separated-Flow Velocity Ratios at  $\alpha = 0^\circ$